Abstract
For the Period Ending June 30, 2022

PROJECT TITLE: Develop Inexpensive Energy from Simple Roll-to-Roll Manufacturing
PROJECT MANAGER: Tianhong Cui
AFFILIATION: University of Minnesota
MAILING ADDRESS: 111 Church Street S.E.
CITY/STATE/ZIP: Minneapolis, MN 55455
PHONE: (612)626-1636
E-MAIL: cuixx006@umn.edu
WEBSITE:
FUNDING SOURCE: Environment and Natural Resources Trust Fund
LEGAL CITATION: M.L. 2018, Chp. 214, Art. 4, Sec. 02, Subd. 07c as extended by M.L. 2021, First Special Session, Chp. 6, Art. 6, Sec. 2, Subd. 18

APPROPRIATION AMOUNT: $300,000
AMOUNT SPENT: $300,000
AMOUNT REMAINING: $0

Sound bite of Project Outcomes and Results
Perovskite solar cells and modules were fabricated via two-step deposition method, hybrid chemical vapor deposition and air blade deposition, to produce electricity from free clean solar energy which reduced dependency on non-renewable energy usage and provides healthy environment and habitats for both residents and wildlife of Minnesota.

Overall Project Outcome and Results
Perovskite material is a promising candidate for the next generation of solar cells with high efficiency and significantly lower cost than silicon solar cells. The final objective of this project is low-cost roll-to-roll manufacturing for perovskite solar cells. Roll-to-roll manufacturing compatible fabrication methods, including hybrid chemical vapor deposition and air blade deposition, were developed. More specifically, chemical vapor deposition processes are optimized, and air blade coating system were developed based on a 3D printer. Perovskite solar cell compositions, structures, and additives were also investigated and optimized to enhance the performance. We developed flexible perovskite solar cells on PEN substrates, which is compatible with roll-to-roll process, and shows an efficiency of 13.3% via chemical vapor deposition method. Device with power conversion efficiency of 13.82% via air blade and chemical vapor deposition methods is also achieved. 5 cm x 5 cm perovskite solar modules with an active area of 18 cm^2 were fabricated and field test was performed. This project shows proof of the concept of CVD grown perovskite solar cells with air blade deposition. The approach shows promising results with high efficiency. Moreover, air blade and CVD deposition techniques can be integrated with roll-to-roll manufacturing systems for large volume production to reduce the overall cost. Even though these techniques are still not ready for deployment, CVD and air blade deposition methods are still recommended for further investigation due to their ease of use, low cost, and large volume production capabilities. Cheap and clean electricity produced from perovskite solar cells via the developed roll-to-roll compatible methods during this project may further benefit the residents of Minnesota. Harvesting green solar energy more efficiently and economically via the development of perovskite techniques can provide and maintain a better living and natural environment for the people of Minnesota.

Project Results Use and Dissemination
The field test was performed on University of Minnesota campus and the findings were disseminated through the following publications in archived journals.

1. Rui Zhu, Xiangyang Wei, Gongnan Xie, Terrence Simon, and Tianhong Cui. "Numerical simulation of vapor deposition process of perovskite solar cells: The influence of methylammonium iodide vapor flow to perovskite growth." *Journal of Solar Energy Engineering* 143, no. 1 (2021).

2. Xiangyang Wei, Yangke Peng, Gaoshan Jing, Terrence Simon, and Tianhong Cui, “High Performance Perovskite Solar Cells Fabricated by a Hybrid Physical-Chemical Vapor Deposition”, ASME Journal of Solar Energy Engineering, Vol. 143, No. 4, 2021: 041006
3. Wei, Xiangyang, Yanke Peng, Gaoshan Jing, and Tianhong Cui. "Planar structured perovskite solar cells by hybrid physical chemical vapor deposition with optimized perovskite film thickness." *Japanese Journal of Applied Physics* 57, no. 5 (2018): 052301.

Environment and Natural Resources Trust Fund (ENRTF)
M.L. 2018 Work Plan Final Report

Date of Submission: August 15, 2022

Final Report

Date of Work Plan Approval: 06/05/2018

Project Completion Date: June 30, 2022

PROJECT TITLE: Develop Inexpensive Energy from Simple Roll-to-Roll Manufacturing

Project Manager: Tianhong Cui

Organization: University of Minnesota

Mailing Address: 111 Church Street S.E.

City/State/Zip Code: Minneapolis, MN 55455

Telephone Number: (612)626-1636

Email Address: cuixx006@umn.ed

Web Address:

Location: Minneapolis, Minnesota

Total ENRTF Project Budget:		
	ENRTF Appropriation:	**$300,000**
	Amount Spent:	**$300,000**
	Balance:	**$0**

Legal Citation: M.L. 2018, Chp. 214, Art. 4, Sec. 02, Subd. 07c as extended by M.L. 2021, First Special Session, Chp. 6, Art. 6, Sec. 2, Subd. 18

Appropriation Language: $300,000 the second year is from the trust fund to the Board of Regents of the University of Minnesota to develop inexpensive, high-efficiency solar energy with simple roll-to-roll advanced manufacturing technology, using new materials such as perovskite to make solar cells. This appropriation is subject to Minnesota Statutes, section 116P.10. This appropriation is available until June 30, 2021, by which time the project must be completed and final products delivered.

M.L. 2021, First Special Session, Chp. 6, Art. 6, Sec. 2, Subd. 18. ENVIRONMENT AND NATURAL RESOURCES TRUST FUND; EXTENSIONS. [to June 30, 2022]

I. PROJECT TITLE: Develop Inexpensive Energy from Simple Roll-to-Roll Manufacturing

II. PROJECT STATEMENT:

The objective of this proposal is to develop cheap clean solar energy based on roll-to-roll manufacturing approach (Figure 1). Perovskite is a brand new materials for the next generation of solar cells under development with very high efficiency and super low cost. The proposed advanced manufacturing is a simple roll-to-roll process using low-temperature physical-chemical deposition of perovskite, which is highly energy-efficient and very inexpensive. Potentially perovskite solar cells are one of the most disruptive renewable energy sources, and the proposed new manufacturing is the key to make it happen eventually. The proposed roll-to-roll manufacturing approach will enable the development of high-performance solar cells with extremely lower cost, compared to silicon solar cells. The success of this proposal will provide renewable green energy as centralized power plants to reduce the imports of energy from foreign countries. In addition, as low-cost distributed energy sources, the perovskite solar cells can be easily adopted by families or individual electronics customers, which will significantly improve the energy efficiency of all economic sectors. Through the proposed roll-to-roll manufacturing, perovskite solar cells can become a truly clean, low-cost, renewable energy source as an effective energy sources in Minnesota State. This project is intended to provide foundational knowledge of the technique and prove its feasibility of cheap perovskite solar cells. In the next phase of the research, we will closely collaborate with state manufacturers and energy providers in Minnesota to further develop an implementation and commercialization plan.

Upon completion of the project, cheap and high-efficiency perovskite solar cells for outdoor solar to electricity conversion will be developed. The knowledge learned throughout the project will provide a solid foundation for further research and development efforts that would lead to implementation of the new solar cells for residential, power plants, or consumer electronics. Eventually, cheap, clean, renewable, and high-efficiency solar energy sources will be installed in Minnesota. In addition to the low-cost of roll-to-roll manufactured solar cells, the cost of transportation, installation and support system will also decrease drastically due to their lighter weight and flexibility. This will potentially provide a supplementary energy solution to current energy sources in Minnesota, ultimately help implement the renewable energy policy, and thus enhance the economic and ecological benefits of Minnesota.

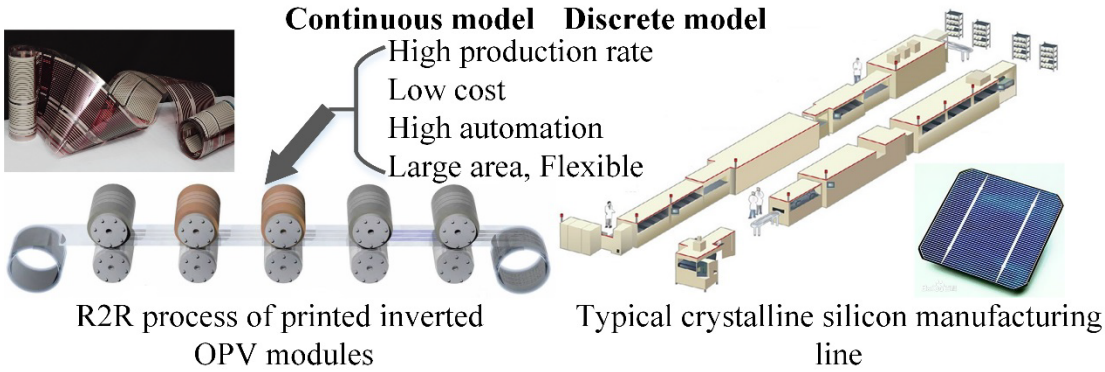

Figure 1. A comparison between roll-to-roll (R2R) manufacturing processes (left) and typical silicon solar cells manufacturing processes (right).

III. OVERALL PROJECT STATUS UPDATES:

Project Update December 31, 2018:

The University of Minnesota team started this project on July 1, 2018. Professors Cui recruited two visiting research assistants conducting the work, while collaborating with Professor Terrence Simon on the modeling of perovskite solar cells. Significant progress has been made. In this report are summaries of progress including a numerical model to analyze the fluid flow and mass transfer in the CVD deposition process of perovskite $MAPbI_3$, set-up of fabrication systems, built-up of a solar cell test system, and initial fabrication of perovskite solar cells. In summary, the initial 6-month work was successful.

Project Update June 30, 2019:

The University of Minnesota team started this project on July 1, 2018. Professors Cui worked with two visiting students, Xiangyang Wei and Rui Zhu, conducting the work, while collaborating with Professor Terrence Simon on the modeling of perovskite solar cells. With the fabrication system including a glove box, a CVD system and some other systems built up already, we fabricated a series of perovskite solar cells based on the mixed perovskite films by a hybrid physical chemical vapor deposition method (HPCVD), which is compatible with the roll-to-roll manufacturing processes. With the optimization of mass ratio of FAI and MABr and the growth temperature in the CVD process, a high efficiency of 15.48% is achieved. The fabrication process is being optimized further to achieve a higher efficiency for now. In addition, the growth process of the surface of perovskite film in the CVD process is also characterized by using AFM, which can help us to improve our designed the roll-to-roll system to fabricate perovskite films. At last, based on the finished results achieved, we demonstrate a designed roll-to-roll manufacturing processes coupled with low temperature chemical-physical vapor deposition for fabrication of perovskite films. In summary, the second 6-month work was productive and successful.

Project Update December 31, 2019:

The University of Minnesota team started this project on July 1, 2018. Professors Cui worked with two Ph.D. students, Jungyoon Kim and Jitong Duan, conducting the work, while collaborating with Professor Terrence Simon and visiting student Rui Zhu on the modeling of perovskite solar cells.
This report includes the preparation of the materials and fabrication of flexible perovskite solar cells. We characterize the surface morphology of the perovskite to check the grain size by atomic force microscopy (AFM) and scanning electron microscopy (SEM). The efficiency of solar cells is measured by the solar simulator. The relationship between efficiency and grain size is also included in the report. In summary, the third 6-month work was productive and successful.

Project Update June 30, 2020:

The University of Minnesota team started this project on July 1, 2018. Professors Cui worked with two Ph.D. students, Jungyoon Kim and Jitong Duan, conducting the work, while collaborating with Professor Terrence Simon on the modeling of perovskite solar cells. This report includes the preparation of the materials and fabrication of perovskite solar cells. We studied the materials to introduce better hole transport layers (HTL) for roll-to-roll perovskite solar cells. PTAA is used as HTL, and the results are

compared with the solar cells using PEDOT:PSS as HTL. The surface morphologies of the perovskite were characterized by atomic force microscopy (AFM). The efficiency of flexible solar cells is measured by the solar simulator. Due to lab closure from March to June 2020, we will conduct more assessment of flexible solar cells compared to silicon solar cells in the next stage. In summary, the third 6-month work was productive and successful.

Project Update December 31, 2020:

The University of Minnesota team started this project on July 1, 2018. Professors Cui worked with one post-doc, Jungyoon Kim, and one Ph.D. student, Jitong Duan, conducting the work, while collaborating with Professor Terrence Simon on the modeling of perovskite solar cells. This report includes the fabrication of flexible perovskite solar cells using SnO_2 as an electron transport layer (ETL) and the comparison of the device performance between ETLs of TiO_2 and SnO_2. The devices was fabricated on different substrates, FTO/glass for TiO_2 and ITO/glass for SnO_2. After we confirm the feasibility of SnO_2 based device on glass, we changed the substrate to ITO/PEN for flexible perovskite solar cells. In the experiment, the perovskite film is synthesized by a low temperature CVD process. The surface morphology of films is characterized by atomic force microscopy (AFM). The efficiency of solar cells is measured by a solar simulator. In summary, although there is some delay on the research progress due to pandemic, we still made some progress in this project.

Project extended to June 30, 2022 by LCCMR 7/1/21 as a result of M.L. 2021, First Special Session, Chp. 6, Art. 6, Sec. 2, Subd. 18, legislative extension criteria being met.

Project Update June 30, 2021:

The University of Minnesota team started this project on July 1, 2018. Professors Cui worked with one post-doc, Jungyoon Kim, and one master student, Yingming Xu, conducting the work. This research includes the optimized fabrication process of perovskite solar cells on a flexible substrate and the coating equipment for roll-to-roll manufacturing. The first objective of this research is optimizing the process for high-efficiency flexible perovskite solar cells. SnO_2 was used for electron transport layers (ETL). The devices were fabricated on ITO/PEN substrate. In the experiment, the perovskite film is synthesized by a low-temperature CVD process. The surface morphology of the films is characterized by atomic force microscopy (AFM). The efficiency of solar cells is measured by the solar simulator. A 3D printer was modified to be a part of the roll-to-roll manufacturing. The printer head and air nozzle were fabricated and attached to the printer. In summary, although there is some delay on the research progress due to pandemic, we still made some progress in this project.

Project Update December 31, 2021:

The University of Minnesota team started this project on July 1, 2018. Professors Cui worked with one post-doc, Jungyoon Kim, and one master student, Yingming Xu, conducting the work. This technical report includes a scalable fabrication process on the flexible substrate and coating techniques for the fabrication of the perovskite solar cells (PSCs) and modules (PSMs). Tetramethylammonium tetrafluoroborate ($[M_4N]BF_4$) is investigated as the post treatment to assist the crystallization of the perovskite film. The perovskite film is synthesized via low temperature CVD process and uniform power conversion efficiencies across different devices are obtained. A 3D printer based slot die coater is built as the coating module of the roll-to-roll manufacturing system and highly uniform SnO_2 and PbI_2 films

are obtained with controllable thicknesses. The 3D slot die coater is further developed into a low-pressure air knife coater to reduce the manufacturing costs and simplify the coating processes. The fabricated films are characterized by atomic force microscopy (AFM) and surface profiler. In summary, although there is some delay on the research progress due to pandemic, we still made some progress in this project.

Final Update June 30, 2022

Perovskite material is a promising candidate for the next generation of solar cells with high efficiency and significantly lower cost than silicon solar cells. The final objective of this project is low-cost roll-to-roll manufacturing for perovskite solar cells. Roll-to-roll manufacturing compatible fabrication methods, including hybrid chemical vapor deposition and air blade deposition, were developed. More specifically, chemical vapor deposition processes are optimized, and air blade coating system were developed based on a 3D printer. Perovskite solar cell compositions, structures, and additives were also investigated and optimized to enhance the performance. We developed flexible perovskite solar cells on PEN substrates, which is compatible with roll-to-roll process, and shows an efficiency of 13.3% via chemical vapor deposition method. Device with power conversion efficiency of 13.82% via air blade and chemical vapor deposition methods is also achieved. 5 cm x 5 cm perovskite solar modules with an active area of 18 cm^2 were fabricated and field test was performed. This project shows proof of the concept of CVD grown perovskite solar cells with air blade deposition. The approach shows promising results with high efficiency. Moreover, air blade and CVD deposition techniques can be integrated with roll-to-roll manufacturing systems for large volume production to reduce the overall cost. Even though these techniques are still not ready for deployment, CVD and air blade deposition methods are still recommended for further investigation due to their ease of use, low cost, and large volume production capabilities. Cheap and clean electricity produced from perovskite solar cells via the developed roll-to-roll compatible methods during this project may further benefit the residents of Minnesota. Harvesting green solar energy more efficiently and economically via the development of perovskite techniques can provide and maintain a better living and natural environment for the people of Minnesota.

Amendment request:
We request changes to the budget in the following amounts: A total of
$257,155 for Personnel, $18,494 in Professional/Technical Contracts,
$24,351 in Equipment/Tools/Supplies, and $0 in Travel. The changes are needed because the COVID extension resulted in more staff time spent on the project, supplies were cheaper than anticipated, and no travels done during pandemic.

Amendment approved by LCCMR 12/20/22

IV. PROJECT ACTIVITIES AND OUTCOMES:

ACTIVITY 1: Development of low-cost roll-to-roll manufacturing for perovskite solar cells
Description: The objective of this activity is to develop cheap advanced manufacturing technique based on roll-to-roll low-temperature processes and to build economical perovskite solar cells accordingly. New perovskite solar cells will be designed and fabricated for high-efficiency solar energy to electricity conversion. Through this new advanced manufacturing, the target is to develop perovskite solar cells with a power conversion efficiency of 15% ~ 25% comparable to silicon solar cells

and the fabrication cost at 1/10 ~ 1/100 of silicon-based solar cells, resulting in an overall installation cost at least 5 times lower than the existing silicon photovoltaics.

We propose to address the following issues of the roll-to-roll manufacturing processes for solar cells: (1) Choosing appropriate flexible substrate materials. (2) Fabricating high-performance functional materials. (3) Integrating a series heterogeneous manufacturing processes. We will come up with solutions for the manufacturing of perovskite solar cells.

Specific tasks will be:

1. Roll-to-roll manufacturing processes set-up, coupled with low-temperature chemical-physical vapor deposition
    a. Design hardware set-up for roll-to-roll manufacturing process based on the chemical-physical vapor deposition facility available at Dr. Cui's Lab
    b. Fabricate and assemble roll-to-roll manufacturing process set-up
    c. Test roll-to-roll manufacturing process set-up

2. Design and experiments of roll-to-roll manufacturing processes for perovskite solar cells
    a. Design roll-to-roll manufacturing processes for perovskite solar cells
    b. Test, characterize and optimize roll-to-roll manufacturing processes for perovskite solar cells

3. Design, fabrication, and characterization of perovskite solar cells in lab using the developed roll-to-roll manufacturing processes
    a. Design and simulate perovskite solar cells using the developed roll-to-roll manufacturing processes
    b. Fabricate solar cells using the developed roll-to-roll manufacturing processes
    c. Characterize solar cells using the developed roll-to-roll manufacturing processes

4. Comprehensive assessment of the new perovskite techniques and silicon solar cells
    a. Assess the design of roll-to-roll processes set-up, and compare to silicon solar cells
    b. Assess the roll-to-roll fabrication techniques of perovskite solar cells, and compare to silicon solar cells
    c. Assess the performance of perovskite solar cells including power conversion efficiency, cost, and stability in lab, and compare to solar cells

Summary Budget Information for Activity 1:

ENRTF Budget: $ 201,002
Amount Spent: $ 201,002
Balance: $ 0

Outcome	**Completion Date**
1. Roll-to-roll manufacturing processes set-up, coupled with low-temperature chemical-physical vapor deposition	*6/30/2019*
2. Design and experiments of roll-to-roll manufacturing processes for perovskite solar cells	*6/30/2019*
3. Design, fabrication, and characterization of perovskite solar cells in lab using the developed roll-to-roll manufacturing processes	*6/30/2020*
4. Comprehensive assessment of the new perovskite techniques and silicon solar cells	*6/30/2020*

Project Update December 31, 2018:

Activity 1 update as of December 31, 2018

Outcome 1: Roll-to-roll manufacturing processes set-up, coupled with low-temperature chemical-physical vapor deposition.

We set up the roll-to-roll manufacturing facility. We fabricated perovskite solar cells using the chemical-physical vapor deposition method. First, we installed a glove box to control humidity because some films are very sensitive to humidity including PbI2, perovskite and Spiro. The air inside the glovebox was exchanged to nitride to meet the low humidity condition. Next, we prepared the solar cell measurement system, which can measure the efficiency of the solar cells.

We also started to establish theoretical modeling of perovskite solar cells to analyze the gas flow during the chemical-physical vapor deposition process because the gas flow is a very important factor for the fabrication. The commercial software ANSYS Fluent is used to do the simulation. We believe that the simulation study helps us to find the optimized condition for the fabrication.

Outcome 2: We have not yet begun work on this because it is dependent on completion of outcome 1.

Outcome 3: We have not yet begun work on this because it is dependent on completion of outcome 2.

Outcome 4: We have not yet begun work on this because it is dependent on completion of outcome 3.

Project Update June 30, 2019:

Activity 1 update as of June 30, 2019

Outcome 2: Design and experiments of roll-to-roll manufacturing processes for perovskite solar cells

Our perovskite solar cells have the structure of FTO/ Electron transport layer (ETL)/ Perovskite film/ hole transport layer (HTL)/ gold electrode. We studied to get better quality perovskite film with mixed precursor materials. In the improved process, a PbI_2 solution was coated on the TiO_2/FTO substrate, and the coated PbI_2 film is baked on a hot plate. Next, the prepared PbI_2/TiO_2/FTO/glass samples are reacted with mixed FAI and MABr during the HPCVD process. We fabricated many samples with different ratios of the two materials to find the optimized ratio for the high-quality film. When we used the mass ratio of FAI and MABr at 95:5, we got very stable and high-quality perovskite film. We did experiments on a flexible polymer using roll-to-roll processes.

In this work, we also tried to find the optimized fabrication temperature and time. The optimal growth temperature and time were 115^{o}C and 7 h, respectively. The fabricated perovskite films were characterized by scanning electron microscopy (SEM) and atomic force microscopy (AFM), which can check the surface shape and roughness. We finally got very low RMS value (19.70 nm) that shows how rough the surface is. The fabricated perovskite solar cell shows a high efficiency of 15.48% (J_{sc} = 22.23 mA/cm^2, V_{oc} = 1.02 V, FF = 0.68).

Outcome 3: We have not yet begun work on this because it is dependent on completion of outcome 2.

Outcome 4: We have not yet begun work on this because it is dependent on completion of outcome 3.

Project Update December 31, 2019:

Activity 1 update as of December 31, 2019

Outcome 3: Design, fabrication, and characterization of perovskite solar cells in lab using the developed roll-to-roll manufacturing processes

We investigated structures and materials for the flexible perovskite solar cells, as it is necessary to use flexible substrate for the roll-to-roll fabrication. First, we changed the traditional planar structure to an inverted structure because the planar structure needs high-temperature process where the flexible substrate cannot survive. Next, we substituted the materials for the inverted structure because we need use proper materials based on the device structure. The inverted structure consists of PEN/ITO/PEDOT:PSS/Perovskite/PCBM/BCP/Ag layers. In this work, we used PEDOT doped with PSS, PCBM, and BCP for the new structure, and tried to find the optimal condition for the fabrication. PEDOT doped with PSS was spin-coated on the patterned ITO/PEN substrate (8000 rpm for 40 s). The substrate was annealed at 120 ℃ for 20 min. PCBM was coated on the perovskite film (2500 rpm for 40 s). Finally, BCP was coated on the PCBM (4000 rpm for 20 s) to help current flow in the device.

We investigated the duration time effect during the fabrication of perovskite film. The perovskite films grew by the HPCVD process for 8 h and 10 h, and we compared the fabricated films to show the duration time effect. We analyzed the surface quality of the perovskite films using AFM and SEM. 10 h process showed a much larger grain size of the perovskite than that in 8 h process. This result shows that we can get a better quality of perovskite film with a 10 h process because larger grain size means fewer defects in the film. Finally, we successfully found a proper structure and materials, and the fabricated solar cells have an efficiency of 7.6%. The structure and materials can be applied to the roll-to-roll manufacturing process.

Outcome 4: We have not yet begun work on this because it is dependent on completion of outcome 3.

Project Update June 30, 2020:

Outcome 4: Comprehensive assessment of the new perovskite techniques and silicon solar cells

We fabricated perovskite solar cells using different hole transport layer (HTL) materials such as AI4083 and PTAA. We grew the perovskite films using CVD process for 10 hours on different HTL films, and we characterized the grown perovskite film using atomic force microscope (AFM). We confirmed that the hydrophobic surface of PTAA makes larger grain size of perovskite by isolating PbI_2 nuclei from each other, and expected better device performance with larger grain size. The power conversion efficiency (PCE) is 7.6 % with AI4083. The PCE of the device with PTAA is 6.4 %. Although the device did not show the enhanced PCE with PTAA, the open-circuit voltage is increased because of the large grains. As decreasing the recombination with the large grains, we can expect the larger V_{oc}. In the research, we confirm that the grain of perovskite can be increased by the PTAA layer and PTAA can be a great candidate for HTL in perovskite solar cells. We will continue this promising work using roll-to-roll process in the next stage. Due to lab closure from March to June 2020, more assessment of flexible solar cells compared to silicon solar cells will be conducted in the next stage.

Project Update December 31, 2020:

We further improved the fabrication of perovskite solar cells on flexible substrates. For the substrates, we prepare FTO/Glass, ITO/Glass and ITO/PEN. First of all, the substrates were cleaned with acetone, isopropyl alcohol, and DI water. Before coating ETL on FTO and ITO, the surface needs to be treated by oxygen plasma for 15 min to enhance the surface energy. TiO_2 solution is prepared by diluting titanium diisopropoxide bis(acetylacetonate) into butanol. After coating the TiO_2 solution on FTO, the next step

is sintering process. The substrate is annealed under 550 ℃ for 5 hours. Because of the high temperature process, we use FTO/Glass instead of ITO/Glass In terms of SnO_2 solution, the solution is prepared by diluting SnO_2 solution into DI water. SnO_2 film only needs 150 ℃ for the annealing process. The SnO_2 solution is coated on ITO/Glass and ITO/PEN substrates. The following fabrication processes are exactly same for all devices. The PbI_2 film convert to perovskite through CVD process with MABr and FAI mixed powder. The ratio is 95:5 or 95 % FAI by weight and 5% MABr by weight. The temperature is increased from room temperature to 140 ℃ for 30 min and maintained at 140 ℃ for 1 h. The spiro solution is prepared by mixing the spiro powder (0.06 mg), chlorobenzene (0.9 ml) and Li-salt ion solution and 4-tert-Butylpyridine. The coating condition is 4000 rpm for 30 s. As the last layer, Ag (120 nm) is deposited for the top electrode by the thermal evaporator. The grain size of ITO is much smaller in the flexible substrate compared to the glass and the following SnO_2 layer also shows much smaller roughness than one on glass. The roughness of SnO_2 on glass is about 1.5 nm but it is about 0.7 nm on PEN substrate. Since the roughness of TiO_2 film is about 5.3 nm, the roughness can be decreased up to 0.7 nm by using SnO_2 instead of TiO_2.

Project Update June 30, 2021:

Perovskite solar cells can be fabricated via many scalable solution coating processes and one of the most promising methods is slot die coating due to its ability to precisely controlling of the film uniformity and thickness, high ink usage efficiency, high coating speed, and compatibility with scalable processes such as roll-to-roll processing. However, commercialized slot-die coaters often only offer one coating direction and require tens of millimeters to liters of precursor ink to fill the hose and the reservoir prior to coating. To address these issues, a 3D printer was modified into a slot die coater due to its minimal precursor ink wastage, the ability to coat complex geometries, and compatibility with the roll-to-roll processing. Moreover, with additional synergistic crystallization methods, such as dry air quenching and substrate heating, uniform dry films can be achieved. This work is to improve the efficiency of roll-to-roll manufacturing process for perovskite solar cells.

Project Update December 31, 2021:

Perovskite solar cells can be fabricated via several scalable methods. Slot die coating technique is shown to be one of the most promising methods that achieve high quality PSCs. Due to its compatibility with the roll-to-roll system, a 3D printer is modified into a 3D slot die coater that achieves precise control of the film thickness and uniformity. Moreover, in order to control the crystallization of the films, dry air quenching is applied during the coating process.

During the testing of the slot die coating, the air quenching is found to mobilize the precursor ink and coating bead formed by the slot die head. According to this phenomenon, a new coating method that utilizes air knife is proposed and tested. Basing on the slot die coating method and dry air quenching, an air knife nozzle is designed and fabricated to replace the slot die head as the main coating element. The dry air is directly used to coat the precursor and assist the crystallization. Unlike the slot die coating technique, the air knife coating module can achieve high-quality and low-cost films that does not require ultraprecise control of the precursor ink distribution via the slot die head.

To further reduce the cost of fabrication,3D slot die coater is redesigned where the mini slot die head is removed, and the dry air nozzle is directly used as the coating element. A stainless-steel blade is attached to the nozzle and the height is set to 100 μm. During the coating process, the blade initially

distributes the precursor solution, and the air knife serves as the primary thickness control element. The film thickness can be directly controlled by the coating speed and the air flowrate. The highest power conversion efficiency exceeds 10% with an average PCE of 8.6%. With the [M4N]BF4 passivation layer, the device-to-device uniformity in improved as shown in Table 1. However, the majority PCEs of the PSCs fall below 10%. In the next stage, more ILs will be tested to improve the power conversion efficiency and stability simultaneously.

Final Update June 30, 2022

The air blade coating system was further studied. A 3D printer is modified as the base platform of the air blade coating system that offers precise control of coating speed and air nozzle height. A stainless-steel blade is attached in the front of the air nozzle to disperse the PbI_2 solution to form an initial wet film of 100 μm. The dry air blade is then scanned over the initially dispersed wet film for drying and reducing the film thickness to 200 to 300 nm. The height of the dry air nozzle is set to 10 mm, and the air flow rate is controlled at 900 SCCM.

To improve the PSC efficiency, additives are further investigated. The first additive is KOH during the formation of SnO_2 film. It was found that the SnO_2 solution consists of KOH that is desirable for highly efficient PSCs. The SnO_2 colloidal solution was diluted from 15 wt% concentration to 2.67 wt% by deionized water. The solution should contain KOH with a desired concentration of 10 mM. The second additive is KI that is added during the PbI_2 film deposition. 10 μM of KI was added to the PbI_2 precursor solution for dry air blade thin film deposition. The final additive is Ionic liquid $[M_4N]BF_4$ that was dissolved in IPA and deposited on CVD perovskite film. However, it was not suitable for CVD developed perovskite layer as the $[M_4N]BF_4$ in IPA would wash out the perovskite film. $[M_4N]BF_4$ was then used as the additive that is introduced to the PbI_2 solution before CVD growing perovskite.

By utilizing the mentioned additives and optimizing the air blade coating parameters, the power conversion efficiency of 13.82% was achieved. The same fabrication procedure was used to fabricate 5 cm x 5 cm perovskite solar modules (PSMs) with an active area of 18 cm^2. The PSMs utilized a parallel structure and silver grids with busbars were deposited to reduce the resistance losses from FTO. Finally, encapsulation modules were designed for the PSMs, and field test was performed.

In summary, even though the airblade deposition and CVD showed poorer performance compared to other coating techniques, such as spin coating and slot die coating in the literature. It is still a very promising approach due to its easiness of use, low cost, and large-scale production capability. The potassium salts, KOH and KI, additives are successful demonstrated to improve the power conversion efficiency, except the ionic liquid $[M_4N]BF_4$. Moreover, perovskite solar modules with active areas of 18 cm^2 was demonstrated and further investigation is recommended.

ACTIVITY 2: Development of perovskite solar cells and field test
Description: A prototype panel of perovskite solar cells will be designed and constructed to demonstrate the feasibility. Field testing protocol and hardware will be developed and tested. Field testing will include setting up a test site in Minnesota. Upon completion of the project, we will demonstrate the perovskite solar cells panel to the stakeholders and LCCMR committee members and officials.

Based on the roll-to-roll manufacturing processes, we will focus on fabricating a prototype panel of perovskite solar cells and field testing of the solar panel. The specific objectives of the development of perovskite solar cells and field testing are (1) to develop a prototype panel of perovskite solar cells based on the fabricated solar cells using roll-to-roll manufacturing, (2) to develop field testing protocol and hardware, and (3) to test real-time solar irradiation of perovskite solar cells by setting up the prototype unit on an outdoor site.

Specific tasks will be:

1. A prototype panel of perovskite solar energy will be developed, based on the fabricated solar cells using roll-to-roll manufacturing
    a. Design prototype perovskite solar panel, based on the fabricated solar cells using roll-to-roll manufacturing techniques
    b. Assemble a prototype perovskite solar panel

2. Field testing protocol and hardware will be developed
    a. Design field testing protocol and hardware for a prototype panel of perovskite solar energy
    b. Characterize the protocol and hardware for a prototype panel of perovskite solar energy on power conversion efficiency and stability

3. The prototype unit will be set up on an outdoor site and real-time solar irradiation of perovskite solar cells will be tested.
    a. Design a field site used to long-term test the prototype unit outdoors. Environmental condition, transmission method and the surroundings will be arranged appropriately for a long-term and precise test.
    b. Develop a system which can test and record the illumination intensity of sunshine and the current-voltage data of the prototype unit running in sunshine outdoors.

Summary Budget Information for Activity 2:

ENRTF Budget: $ 98,998
Amount Spent: $ 98,998
Balance: $ 0

Outcome	Completion Date
1. A prototype panel of perovskite solar energy will be developed, based on the fabricated solar cells using roll-to-roll manufacturing	*6/30/2022*
2. Field testing protocol and hardware will be developed	*6/30/2022*
3. The prototype unit will be set up on an outdoor site and real-time solar irradiation of perovskite solar cells will be tested.	*6/30/2022*

Project Update December 31, 2018:

N/A

Project Update June 30, 2019:

N/A

Project Update December 31, 2019:

N/A

Project Update June 30, 2020:

N/A

Project Update December 31, 2020:

Outcome 1: A prototype panel of perovskite solar energy will be developed, based on the fabricated solar cells using roll-to-roll manufacturing

We fabricated flexible perovskite solar cells using SnO_2 as an electron transport layer (ETL) and compared the device performance of solar cells using TiO_2 and SnO_2 as ETLs. We fabricated the devices on different substrates, FTO/glass for TiO_2 and ITO/glass for SnO_2. After we confirmed the feasibility of SnO2 based device on glass, we changed the substrate to ITO/PEN for flexible perovskite solar cells. In the experiment, we synthesized the perovskite film using a low temperature CVD and roll-to-roll processes. We characterized the surface morphology of films by an atomic force microscopy (AFM). We measured the efficiency of solar cells with a solar simulator. The power conversion efficiencies of perovskite solar cells are 15.43 % and 15.64 % with TiO_2 and SnO2 on glass, respectively. The power conversion efficiency of flexible solar cells is 8.7%. Although the flexible device shows a lower efficiency than glass substrate, we believe that the performance of flexible solar cells can be enhanced by an optimization in the next phase. In summary, although there is some delay on the research progress due to pandemic, we made some progress in this project. We applied for a no-cost extension for one more year to finish the overall project.

Outcome 2: We have not yet begun work on this because it is dependent on completion of outcome 1.

Outcome 3: We have not yet begun work on this because it is dependent on completion of outcome 2.

Project Update June 30, 2021:

Outcome 1: A prototype panel of perovskite solar energy will be developed, based on the fabricated solar cells using roll-to-roll manufacturing

Perovskite solar cells were developed on flexible substrate successfully. Many research groups have been focused on perovskite solar cells among several types of solar cells because of their high performance. Traditionally, TiO_2 is used for the electron transport layer (ETL) due to its proper bandgap and work function for solar cells. However, there is an issue that we must tackle. Since the TiO_2 needs a high temperature (about 550 ℃) sintering process to get the electrical properties, it is necessary to find another candidate which does not need the high-temperature process. A SnO_2 can be a great candidate for the because we can get down the annealing temperature to 150 ℃. SnO_2 also has a wider bandgap, higher conductivity and greater optical transparency than TiO_2. As a result, we can expect the high efficiency of the device with SnO_2. The morphology is characterized by atomic force microscopy and the performance of the device is measured by a solar simulator. In the research, we used SnO_2 for the ETL

in perovskite solar cells instead of TiO_2. ITO/PEN substrates were used for the flexible substrate. The perovskite films grew by the CVD process on the ETL film and the surface morphology was characterized by AFM. The fabricated devices are evaluated by a solar simulator and the results show that SnO_2 is a great candidate for ETL. The champion device has 13.3 % efficiency.

Outcome 2: We have not yet begun work on this because it is dependent on completion of outcome 1.

Outcome 3: We have not yet begun work on this because it is dependent on completion of outcome 2.

Project Update December 31, 2021:

Outcome 1: A prototype panel of perovskite solar energy will be developed, based on the fabricated solar cells using roll-to-roll manufacturing

The 3D slot die coater is redesigned, where the mini slot die head is removed, and the dry air nozzle is directly used as the coating element. This process is also applied to fabricate large area (10 x 10 cm) perovskite solar modules (PSMs). Au grids are designed on top of the PSMs to collect the electrons efficiently. Since the area of the perovskite film is significantly larger, the CVD fabrication process need to be further optimized to improve the quality.

To achieve high quality perovskite films with large surface areas, slot die coating technique is investigated. The 3D printer modified slot die coater is used to deposit SnO_2 and PbI_2 films. The slot die head to substrate height, coating speed, and precursor feed rate are first optimized. For the head to substrate height of 100 µm and constant ink feed rate of 130 µL/min, the coating speed can be increased up to 1200 mm/min. To reduce the fabrication time, a higher coating speed is desired. However, as the coating speed increases, the viscous force caused by the ink becomes more significant, thus higher thickness film can be fabricated. The optimized coating speed to fabricate SnO_2 film is found to be 800 mm/min. The 3D slot die coated SnO_2 film shows desired surface coverage and low RMS surface roughness of 15.53 nm that is comparable to the spin coated SnO_2 film. Similar procedures are carried out to optimize the PbI_2 film. Since the coating module needs to be compatible with the roll-to-roll systems, constant coating speed is desired throughout the whole fabrication process. Therefore, the same coating speed of 800 mm/min is used to fabricate the PbI_2 film and the thickness is easily controlled by adjusting the PbI_2 concentration. To assist the PbI_2 crystallization, a dry air quenching module is implemented to extract the PbI_2 from the solvent. Small-scale (2 x 2 cm) film and continuous large-scale film (2 x 10 cm) are fabricated with the dry air quenching assistance.

Outcome 2: We have not yet begun work on this because it is dependent on completion of outcome 1.

Outcome 3: We have not yet begun work on this because it is dependent on completion of outcome 2.

Final Update June 30, 2022

Outcome 1: A prototype panel of perovskite solar energy will be developed, based on the fabricated solar cells using roll-to-roll manufacturing

Outcome 2: Field testing protocol and hardware will be developed.

Outcome 3: The prototype unit will be set up on an outdoor site and real-time solar irradiation of perovskite solar cells will be tested.

The highest power conversion efficiency (PCE) via spin coating and chemical vapor deposition methods was enhanced from 8.59% to 9.45%. However, no significant enhancements were made with the ionic liquid $[M_4N]BF_4$ due to its low solubility in the solvent, DMF and DMSO, during PbI_2 deposition.

To achieve roll-to-roll manufacturing of the PSCs, dry air blade coating technique was further investigated. PbI_2 film was first deposited via dry air blade coating method and uniform film with low roughness of 3.4 nm was obtained. The air blade deposited PbI_2 film showed desired surface characteristics that was comparable to the spin coating method. The dry air quickly extracted the solvent and distributed thick wet film, thus forming uniform PbI_2 films to serve as the growing seeds for the perovskite film during CVD process.

Air blade deposited PbI_2 film was moved to undergo seven hours of perovskite growth process under 115 ℃ in vacuum and was cooled to room temperature with a rate of 0.7 ℃/minute. PbI_2 film reacted with FAI and MABr during CVD process and was fully converted into black perovskite. The developed perovskite film exhibited promising film qualities with high smoothness and uniformity. The average size of perovskite grains is more than 500 nm with some grain sizes near 1 µm. After incorporating KI, KOH, and $[M_4N]BF_4$ additives, defects in the perovskite film were reduced. The power conversion efficiency of air blade fabricated champion devices was enhanced to 13.82 %, whereas the spin coated PSC from the same batch of fabrication achieved a lower PSC of 8.3%. However, the air blade fabricated PSCs can still be improved by improving the interface between perovskite and SnO_2 films.

Perovskite solar modules were also fabricated. PSMs showed a size of 5 cm x 5 cm with four light absorbing subcells with a total active area of 18 cm^2. The four subcells are laid in parallel to each other to simplify the fabrication process. However, the conventional parallel structure exhibits low power conversion efficiency due to the high resistance of the base transparent conductive oxide layer, such as FTO. Therefore, silver grids were deposited to minimize the distance that the generated electrons must travel in FTO to reduce the resistance losses. The PSMs were encapsulated by PMMA board, and sealed by epoxy to eliminate any undesired effects of moistures and gases in the atmosphere. Measurement system consists of an electrochemical station and a computer. The PSMs were setup for field test. They consist of two copper strips directly connected the exposed silver coated FTO and silver coated Spiro-OMeTAD respectively to form a closed loop.

The approach shows promising results with high efficiency. Moreover, air blade and CVD deposition techniques can be integrated with roll-to-roll manufacturing systems for high volume production to reduce the overall cost. Even though these techniques are still not ready for deployment. CVD and air blade deposition methods are still recommended for further investigation due to their ease of use, low cost, and large volume production capabilities.

V. DISSEMINATION:

Description:

The findings will be disseminated through:

(1) On site demonstration as described in the activities

(2) Public seminars

(3) Progress update on www.me.umn.edu/labs/tianlab
(4) Presentations at national and international technical conferences
(5) Communications with interested entrepreneurs
(6) Peer reviewed papers
(7) Collaboration with Solar Cell Manufacturers

The technologies, if demonstrated successfully, may be implemented to many fields and residentials in the State of Minnesota and beyond. Any intellectual properties and related revenues as a result of the program will be shared between UMN and LCCMR.

Project Update December 31, 2018:

N/A

Project Update June 30, 2019:

N/A

Project Update December 31, 2019:

N/A

Project Update June 30, 2020:

One peer reviewed paper was accepted for a publication by an archived journal:
Rui Zhu, Xiangyang Wei, Gongnan Xie, Terrence Simon and Tianhong Cui, "Numerical simulation of vapor deposition process of perovskite solar cells: the influence of MAI vapor flow to perovskite growth", *ASME Journal of Solar Energy Engineering* (Accepted)

Project Update December 31, 2020:

One peer reviewed paper was accepted for a publication by an archived journal:
Xiangyang Wei, Yangke Peng, Gaoshan Jing, Terrence Simon and Tianhong Cui, "High Performance Perovskite Solar Cells Fabricated by a Hybrid Physical-Chemical Vapor Deposition", *ASME Journal of Solar Energy Engineering* (Accepted)

Project Update June 30, 2021:

N/A

Project Update December 31, 2021:

One peer reviewed paper was published for a publication by an archived journal:
Xiangyang Wei, Yangke Peng, Gaoshan Jing, Terrence Simon, and Tianhong Cui, "High Performance Perovskite Solar Cells Fabricated by a Hybrid Physical-Chemical Vapor Deposition", ASME Journal of Solar Energy Engineering, Vol. 143, No. 4, 2021: 041006

Final Update June 30, 2022

N/A

Final Report Summary

The field test was performed on University of Minnesota campus and the findings were disseminated through the following publications in archived journals.

1. Rui Zhu, Xiangyang Wei, Gongnan Xie, Terrence Simon, and Tianhong Cui. "Numerical simulation of vapor deposition process of perovskite solar cells: The influence of methylammonium iodide vapor flow to perovskite growth." *Journal of Solar Energy Engineering* 143, no. 1 (2021).
2. Xiangyang Wei, Yangke Peng, Gaoshan Jing, Terrence Simon, and Tianhong Cui, "High Performance Perovskite Solar Cells Fabricated by a Hybrid Physical-Chemical Vapor Deposition", ASME Journal of Solar Energy Engineering, Vol. 143, No. 4, 2021: 041006
3. Wei, Xiangyang, Yanke Peng, Gaoshan Jing, and Tianhong Cui. "Planar structured perovskite solar cells by hybrid physical chemical vapor deposition with optimized perovskite film thickness." *Japanese Journal of Applied Physics* 57, no. 5 (2018): 052301.

VI. PROJECT BUDGET SUMMARY:

A. ENRTF Budget Overview: See attached budget spreadsheet

Explanation of Use of Classified Staff: N/A

Explanation of Capital Expenditures Greater Than $5,000: N/A

Number of Full-time Equivalents (FTE) Directly Funded with this ENRTF Appropriation: 0.61 FTE

Number of Full-time Equivalents (FTE) Estimated to Be Funded through Contracts with this ENRTF Appropriation: 0

B. Other Funds:

Source of Funds	$ Amount Proposed	$ Amount Spent	Use of Other Funds
The university overhead unpaid	$137,587	$0	Develop Inexpensive Energy from Simple Roll-to-Roll Manufacturing
TOTAL OTHER FUNDS:	**$137,587**	**$0**	

VII. PROJECT STRATEGY:

A. Project Partners:

Tianhong Cui, professor in Department of Mechanical Engineering and affiliated graduate faculty in Department Electrical and Computer Engineering, will serve as PI and project manager. He will be responsible for overseeing the project, all reports, and deliverables. He will also design the roll-to-roll manufacturing processes and perovskite solar cells based on the advanced manufacturing technique. Under Professor Cui's supervision, the Ph.D. student will be responsible for the manufacturing facility and the outdoor experimental test set-up, and he will also be in charge of design, fabrication, and characterization of perovskite solar cells.

B. Project Impact and Long-term Strategy:

Given the state's latitude, many people are surprised to learn that Minnesota has annual solar radiation similar to portions of Florida and Texas, with sunshine for about 5 hours per day in average in Minneapolis. Solar energy production is a small but exponentially growing resource in Minnesota, where we now have more than 15 Megawatts (MW) of solar electric capacity. In May 2013, the Minnesota legislature adopted a mandate on investor-owned utilities in the state that requires them to produce 1.5% of their electricity from solar power by 2020. The Minnesota Legislature established a solar photovoltaic and solar thermal incentive program for consumers who install photovoltaic and solar thermal systems using solar modules and collectors certified as manufactured in Minnesota.

Solar energy out-powers anything that human technology could ever produce. However, today's commercial solar cells, most often made from silicon, typically convert sunlight into electricity with an efficiency of about 10 percent to 20 percent, although some test cells do a little better. Given their manufacturing costs, modules of today's cells incorporated in the power grid would produce electricity at a cost roughly 3 to 6 times higher than current prices. To make solar economically competitive, engineers must find ways to lower their manufacturing costs and to improve the efficiency of the cells. This project will provide one solution for lowering the cost and improving solar efficiency is to use new materials perovskite together with low-cost roll-to-roll advanced manufacturing techniques.

Upon completion of the project, cheap and high-efficiency perovskite solar cells for outdoor solar to electricity conversion will be developed. The knowledge learned throughout the project will provide a solid foundation for further research and development efforts that would lead to implementation of the new solar cells for power plants or consumer electronics enabling very cheap, clean, renewable, and high-efficiency solar energy sources in Minnesota eventually. This will potentially provide a supplementary energy solution to current energy sources in Minnesota, ultimately help implement the renewable energy policy, and thus enhance the economic and ecological benefits of Minnesota.

C. Funding History:

Funding Source and Use of Funds	Funding Timeframe	$ Amount
Mocon Inc., Graphene gas sensors	Nov. 2014 - July 2016	$173,199
Alexandria Extrusion Inc., Microstructures for Heat Transfer	Nov. 2011 - Dec. 2015	$165,516
DARPA, MEMS-Based Active Heat Sink Technology	Jan. 2009 - Sept. 2013	$2,579,025
MN Partnership, Nano-Sensors	Jan. 2010 – Dec. 2012	$637,500

VIII. REPORTING REQUIREMENTS:

- The project is for 4 years, will begin on 07/01/18, and end on 06/30/22.
- Periodic project status update reports will be submitted *[06/30]* and *[12/31]* of each year.
- A final report and associated products will be submitted between June 30 and August 15, 2022.

IX. VISUAL COMPONENT or MAP(S):

N/A

X. FEE TITLE ACQUISITION/CONSERVATION EASEMENT/RESTORATION REQUIREMENTS:

N/A

Appendix: Visual Component

Project Title: Develop Inexpensive Energy from Simple Roll-to-Roll Manufacturing (160-E)

Current Silicon Solar Cell Production Line from CETC (Very Complex and Expensive)

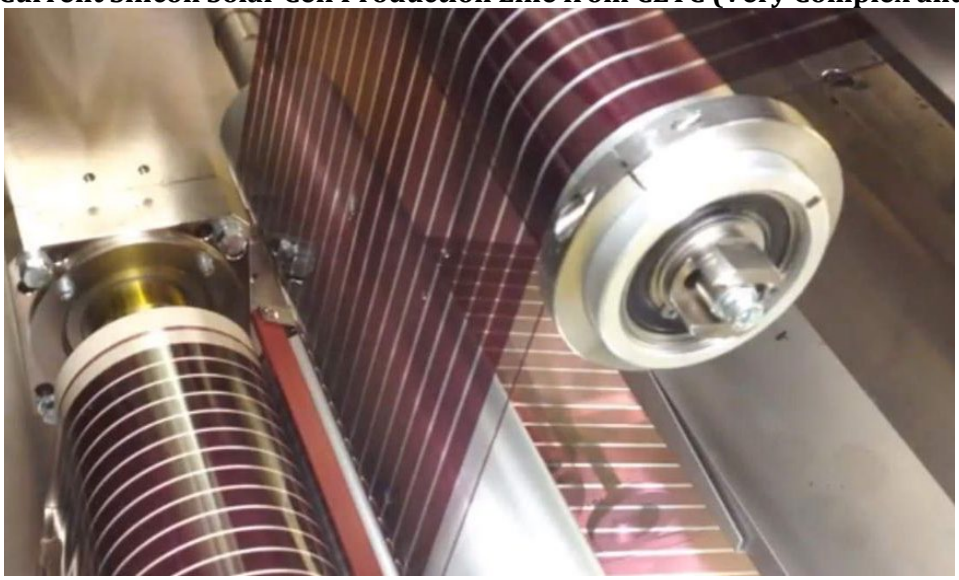

Proposed Roll-to-Roll Processing of Perovskite Solar Cells (Very Simple and Cheap)

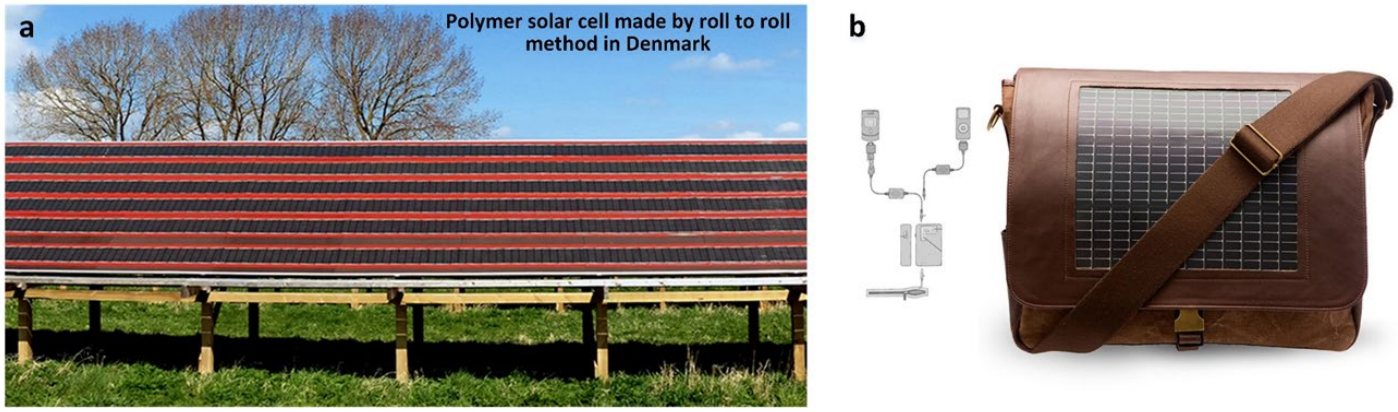

Future Applications of Proposed Cheap Solar Cells (Cheap, Clean, and Renewable)
(a) Solar Power Plant, (b) Soar Powered Consumer Electronics

In-lab fabricated 5 cm x 5 cm perovskite solar modules and field test setup

(a) & (b) perovskite solar panel vs silicon solar panel, (c) front view of perovskite solar panel encapsulation module, (d) back view of the perovskite solar panel encapsulation module, (e) & (f) perovskite solar panel field test

Environment and Natural Resources Trust Fund
M.L. 2018 Budget Spreadsheet - FINAL

Project Title: Develop Inexpensive Energy from Simple Roll-to-Roll Manufacturing
Legal Citation: M.L. 2018, Chp. 214, Art. 4, Sec. 02, Subd. 07c
Project Manager: Tianhong Cui
Organization: University of Minnesota
College/Department/Division: College of Science and Engineering, Mechanical Engineering
M.L. 2018 ENRTF Appropriation: M.L. 2018, Chp. 214, Art. 4, Sec. 02, Subd. 07c
Project Length and Completion Date: Four years - June 30, 2022
Date of Report: Actuals through 8/9/22

ENVIRONMENT AND NATURAL RESOURCES TRUST FUND BUDGET	Total Budget	Amount Spent	Balance
BUDGET ITEM			
Personnel (Wages and Benefits) - Overall	$257,155	$257,155	$0
Dr. Tianhong Cui, PI, 1 month summer salary (11% FTE) & 33.5% fringe for 3 years (Total estimated amount $70,903)			
Graduate Research Assistant, 50% FTE (fall & spring semesters include 16.9% fringe plus $18.94/hour tuition, summer 15% fringe only) for 3 years (Total estimated amount $144,562)			
Professional/Technical/Service Contracts			
Scientific Services: User fees at Minnesota Nano Center and Characterization Facility at the University of Minnesota. The cost is about $875 per month for the research assistant for 3 years.	$18,494	*$18,494*	$0
Equipment/Tools/Supplies			
Lab Materials & Supplies: fabrication materials & supplies including silicon wafers ($8,000), polymer substrates ($9,000), chemicals ($9,035), roll-to-roll manufacturing set-up items ($16,000), bottles, gloves, other electronics for testing, etc. ($6,000)	*$24,351*	*$24,351*	$0
Travel expenses in Minnesota			
Travel- Cui Domestic travel year 2 & 3: Mileage, lodging, and meals for travel to and between the solar testing sites and the university based on the university compensation policy	*$0*	*$0*	$0
COLUMN TOTAL	$300,000	$300,000	$0

Rui Zhu
School of Marine Science and Technology,
Northwestern Polytechnical University,
Xi'an 710072, China
e-mail: ruizhu@mail.nwpu.edu.cn

Xiangyang Wei
State Key Laboratory of Precision Measurement
Technology and Instruments,
Department of Precision Instrument,
Tsinghua University,
Beijing 100084, China
e-mail: wei-xy14@mails.tsinghua.edu.cn

Gongnan Xie
School of Marine Science and Technology,
Northwestern Polytechnical University,
Xi'an 710072, China
e-mail: xgn@nwpu.edu.cn

Terrence Simon
Department of Mechanical Engineering,
University of Minnesota,
Minneapolis, MN 55455
e-mail: simon002@umn.edu

Tianhong Cui[1]
Department of Mechanical Engineering,
University of Minnesota,
Minneapolis, MN 55455
e-mails: cuixx006@me.umn.edu;
cuixx006@umn.edu

Numerical Simulation of Vapor Deposition Process of Perovskite Solar Cells: The Influence of Methylammonium Iodide Vapor Flow to Perovskite Growth

This paper presents a two-dimensional (2D) transient numerical model for simulating the vapor deposition process for growing perovskite films. The diffusion process of methylammonium iodide (MAI) vapor through the processing chamber to react with the lead iodide (PbI_2) substrate and grow the perovskite layer is analyzed with a diffusion coefficient that has been determined by measuring thicknesses of perovskite layers grown in a chemical vapor deposition (CVD) chamber. Innovations applied to the CVD chamber to improve the uniformity of layer thickness and offer control over the growth process are applied and computationally assessed. One is the addition of screens at various strategic locations in the chamber to improve flow uniformity. Another is changing the locations of MAI sublimation bowls and chamber outlet numbers and locations. The results show that adding screens makes the MAI vapor flow more uniform in the plenum while allowing a quicker purge of the N_2 inert gas. This leads to a higher and more uniform growth rate of perovskite. The MAI vapor flow is influenced by the reaction plenum geometry, so the chamber is expected to allow good control of the process to achieve uniform surface deposition rate and controlled grain growth of the perovskite layer. [DOI: 10.1115/1.4047296]

Keywords: perovskite solar cells, chemical vapor deposition, perovskite layer growth, surface deposition rate, transient numerical simulation, efficiency, solar

1 Introduction

Perovskite solar cells have drawn tremendous attention because of their excellent properties such as tunable bandgap, long carrier diffusion length, excellent light absorption performance, low cost, low-temperature processing, and flexible materials. The power conversion efficiency (PCE) of perovskite solar cells has rapidly improved from 3.8% to 25.2% in recent years [1,2], which is close to the best single crystalline silicon solar cells. The next step for researchers is to develop a low-cost and large-scale processing procedure for large-area, high-performance, and stable perovskite solar cell fabrication to make this technology more competitive in commercial applications than for other solar cells, like silicon-based solar cells, CdTe-based solar cells, and so on.

There are many factors that have significant impacts on perovskite solar cell performance, including the perovskite film morphology, crystallinity, thickness, and material purity. To produce high-quality, uniform perovskite films with fewer defects, different kinds of methodologies have been developed, such as the one-step solution method [3–5], the two-step solution method [6,7], the vapor-assisted solution process [8,9], dual-source vacuum deposition [10,11], and hybrid deposition [12]. Among these methodologies, the solution processes are the most popular, and high efficiencies are achieved. However, the solution processes have high uncertainties in the process, making commercial applications challenging. The vapor-assisted deposition technique has more effective control over the working conditions, like pressure, temperature, and heat and mass transfer, which is beneficial for achieving stable and high-performance perovskite solar cells. Besides, as precursor organic and inorganic materials have different boiling points, the vapor-assisted deposition method is more controllable than the dual-source vapor deposition method. Overall, the vapor-assisted hybrid physical–chemical deposition method is more favorable for its higher stability and controllability and higher possibility for commercial application.

Yang and coworkers introduced the methylammonium iodide (MAI) vapor-based approach and named it as vapor-assisted solution processing for the fabrication of the perovskite layer [13–15]. In the process, PbI_2 substrates were reacted with MAI vapor at 150 °C in an N_2 environment for 2 h. The perovskite layers they produced show high crystallinity, large grain size, and uniform surface coverage. The high-quality $CH_3NH_3PbI_3$ perovskite films enhanced the performance of the solar cells from their device with a PCE of 12.1%. Wang et al. [16] systematically studied how the chemical vapor deposition (CVD) process affects the perovskite film property. They changed the substrate temperature, the postannealing condition, and the evaporation source materials. In their experiments, the CH_3NH_3I quartz crystal microbalance (QCM) was placed facing downward and directly above the CH_3NH_3I vapor source. There was a shutter between the CH_3NH_3I QCM and the MAI source to better control the MAI evaporation rate during a long deposition period (1 h). Their results showed that the vapor-assisted deposition process needed careful control and when optimized led to the fabrication of the high-quality perovskite film. The evaporation rate of MAI (CH_3NH_3I) is an important factor in this process, but needs better control during the formation of perovskite.

Lower working pressure leads to a higher sublimation rate of organic halide and a larger diffusion rate, which increases the deposition rate and the uniformity of the perovskite growth. Leyden et al. [17] used a two-step CVD method to grow perovskite

[1]Corresponding author.

Contributed by the Solar Energy Division of ASME for publication in the JOURNAL OF SOLAR ENERGY ENGINEERING: INCLUDING WIND ENERGY AND BUILDING ENERGY CONSERVATION. Manuscript received January 8, 2020; final manuscript received May 18, 2020; published online June 26, 2020. Editor: S. A. Sherif.

films with low working pressure. A two-zone furnace was used in their study. The MAI precursor was placed in one zone with a temperature of 185 °C, while the substrates are placed in the other zone with a lower temperature of 145–170 °C. The working pressure was 100 Pa, and nitrogen was used as the carrier gas. The two-zone furnace increased the deposition rate because the vapor pressure of the organic halide could be controlled independently. The reported nominal reaction time was 1 h. The same group used formamidinium iodide to fabricate perovskite solar cells with a heating time of the organic components of less than 30 min [18]. The best PCE reported is 14.2%. Low pressures also reduce the required reaction temperature, since the sublimation temperature of an organic halide is reduced at lower pressures. Peng et al. [19] used the hybrid vapor-assisted method and fabricated high-performing cells with a PCE of 14.7%. Both their working pressure and temperature are low: 0.3 Pa and 82 °C, respectively. Their study showed that low pressure can reduce the reaction temperature since the sublimation rate of MAI decreases with lower pressure. However, low working pressure and temperature increase the required reaction time.

The performance of a perovskite solar cell is highly influenced by the crystalline quality of the perovskite thin film sandwiched between electron and hole transport layers in a typical perovskite solar cell structure. The crystalline quality is characterized by the crystal grain size and the uniformity of film thickness [20,21]. Although many studies have been done recently on lead halide perovskite nanocrystals, there are still significant gaps in understanding of nucleation and growth processes involved in the formation of perovskite, as well as the relationship between the perovskite crystal structure and the solar cell performance. Agrafiotis et al. [22] tested the thermochemistry properties including the reaction enthalpy of Ca-Mn-based perovskites. Udayabhaskararao et al. [23] used $CsPbX_3$ as a model system to study the formation mechanism of cubic $CsPbX_3$ nanocrystals, their growth via oriented attachment into larger nanostructures, and their associated phase transformations. It was found that the formation of $CsPbX_3$ nanocubes occurs through the seed-mediated nucleation method, where Pb nanoparticles formed during the reaction act as seeds. Further growth occurs through self-assembly and oriented attachment.

The processing temperature and pressure are critical to the formation of uniform and stable perovskite films. Xue et al. [24] conducted a Monte Carlo simulation to study the influence of device geometry, material properties, and operating conditions on the performance of a perovskite solar cell. It was found that the hole mobility in the hole transport layer and the layer thicknesses of the hole and electron transfer layers are the three most important parameters influencing the performance of perovskite solar cell. Yang et al. [25] numerically studied the influence of operating pressure and temperature on the surface deposition rate of perovskite films. The results show that the increasing operating temperature and pressure will increase the surface deposition rate of perovskite. An optimized mass flow configuration was proposed by adding a flow resistance to give a more uniform distribution of MAI vapor flow inside the reaction chamber. Arivazhagan et al. [26] studied the influence of pressure in the CVD process and found that the operating pressure has strong effects on the grain size of the grown perovskite film. They also proposed a method to enhance the perovskite grain size by a gradual change in vapor pressure.

Perovskite solar cells have been rapidly developing in recent years. Currently, the vapor-assisted deposition process is the best way to achieve large and high-quality perovskite films. The process has the advantage of lower temperature processing than used with spin coating. This gives more flexibility in choices for materials for the remainder of the cell, including flexible materials. This article continues to study the vapor deposition process of the perovskite layer by numerical simulation. In this work, hybrid physical–chemical vapor deposition of planar methylammonium lead iodide ($MAPbI_3$) is grown using a MAI precursor vapor. The diffusion process of MAI vapor through the growing perovskite layer is analyzed with a diffusion coefficient calculated by measuring the thickness of the perovskite layer with different growing times. The influences of adding screens at different locations in the plenum and changing the inlet and outlet numbers and locations on the uniformity of the perovskite layer growth rate are analyzed by using computational fluid dynamics and mass transfer. This study helps understand the physics of the vapor deposition process of the perovskite film growth and provide a method to predict and control the surface deposition rate by controlling the working conditions.

2 Numerical Model

2.1 Physical Model and Boundary Conditions. In the reactor, a quartz box is put inside a chamber heated by surrounding heating elements to realize temperature control during the sublimation process. The chamber is first evacuated to a desired pressure, and then nitrogen (N_2) is introduced into the chamber to purge the particles and atmospheric gases. Then the nitrogen flow is shut down, and the heating element is turned on to heat the quartz box to a specific temperature, while a low near-vacuum pressure is maintained in the box. During the heating process, MAI powder in the crucibles sublimates into the quartz box and then mixes and diffuses within the N_2 atmosphere. The mixture of MAI and N_2 flows around the substrate surfaces, which are coated with PbI_2, and then to an outlet. A deposition reaction takes place on the substrate surface, and a layer of perovskite is formed. As the MAI powder continues to sublimate, the quartz box becomes filled with MAI vapor, while the N_2 from its initial charge is purged, finally reaching a steady-state with a steady outflow of pure MAI and a continuous MAI concentration for deposition into the perovskite film on each substrate surface.

To simulate this process, a simplified 2D transient model is established, as shown in Fig. 1. The reaction plenum is a rectangular box with a length of 156 mm and a height of 60 mm. It has three inlets and three outlets. Each inlet is 20 mm wide and 10 mm high, and each outlet is 5 mm wide and 5 mm high. Two screens are put in the plenum, as the figure shows, to make the flow from upper plenum to lower plenum more uniform. The two substrates are 10 mm above the second screen, and each substrate is 20 mm wide and 2 mm thick. The box is initially filled with N_2. From the beginning of the simulation, pure MAI vapor is introduced through the inlets, simulating the sublimation process of the actual system. The N_2 is purged, and finally, the box is filled with MAI vapor. The two substrates are initially coated with PbI_2. The reaction is on the surfaces of the PbI_2 substrates when MAI vapor becomes available.

The computational mesh used in this study is made by ANSYS ICEM 18.2. The mesh has 26,111 nodes, verified to be enough by a mesh-independence test. The commercial computational fluid dynamics software ANSYS FLUENT 18.2 is used for this numerical simulation. The operating pressure and the temperature are set as

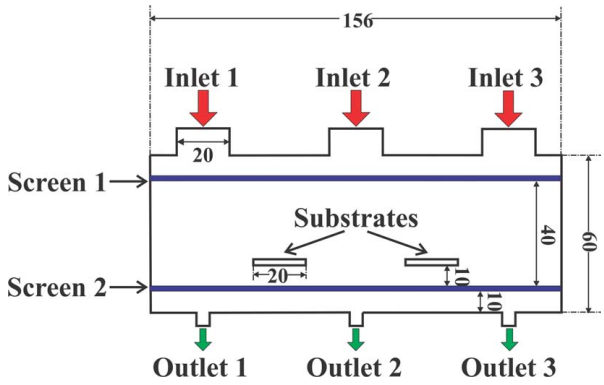

Fig. 1 The geometry of the numerical model used in the simulation

Table 1 Material property of MAI, PbI_2, and perovskite $MAPbI_3$ [25]

	MAI	PbI_2	$MAPbI_3$
Density (kg/m^3)	Idea gas	6160	4000
Specific heat (J/kg K)	498	173	304.85
Thermal conductivity (W/m K)	0.00672	0.73	0.5
Viscosity (kg/m s)	1.243×10^{-5}	1×10^{20}	1×10^{20}
Molecular weight (g/mol)	159	461	620
Standard state enthalpy (J/kmol)	-3.3×10^{-8}	-2.03×10^{-8}	-5.07×10^{-8}
Standard state entropy (J/kmol K)	250,000	174,850	200,000
L-J characteristic length (angstrom)	5.2	5.5	6
L-J energy parameter (K)	478.3	400	550

0.4 Torr (53.33 Pa) and 378.15 K (105 °C), respectively. The properties of MAI vapor are estimated using the Joback estimating approach [27]. The properties of PbI_2 and $MAPbI_3$ are adapted from the literature [28,29]. Table 1 lists the material property used in this study. The inlet condition is set as a pressure inlet with a constant total pressure of 0.1 Pa. The outlets are set with pressure outlet conditions. All the walls are of a constant and uniform temperature. The screens are set as porous-jump boundaries. The porous-jump boundary is a one-dimensional simplification of the porous media model used to model pressure drops through screens. The pressure change is defined as a combination of Darcy's law and an additional inertial loss term:

$$S_i = \sum_{j=1}^{3} D_{ij}\mu v_j + \sum_{j=1}^{3} C_{ij}\frac{1}{2}\rho|v_j|v_j \tag{1}$$

where μ is the viscosity, v is the velocity of the approach flow to the screen, ρ is the density, and D and C are prescribed matrices for Darcy and inertial coefficients, respectively, of the modified Darcy equation.

For a uniform porous medium, Eq. (1) can be simplified as follows:

$$S_i = \frac{\mu}{k}v_i + C_2\frac{1}{2}\rho|v_j|v_j \tag{2}$$

where k is the permeability and C_2 is the inertial resistance factor. In a laminar flow with very low Reynolds number, the inertial loss term is negligible. The permeability is calculated by an empirical formula based on the screen type, opening ratio, and thickness [30], which is 3×10^{-7} m^2 in this study.

Six cases are analyzed to characterize the flow field, diffusion, and mixing processes of MAI vapor during the deposition process. The MAI diffusion through the perovskite layer to the reaction layer and the perovskite growth rate are also analyzed. Furthermore, the analysis helps assess the effectiveness of screens toward making the surface deposition rate of $MAPbI_3$ (perovskite) uniform over the substrates. For cases 1–4, all three inlets and only the middle outlet are open. Case 1 has no screen. Case 2 has the upper screen (screen 1), while case 3 has the lower screen (screen 2). Case 4 has two screens (screens 1 and 2). Both cases 5 and 6 have two screens (screens 1 and 2). For case 5, inlets 1 and 3 and outlet 2 are open, while for case 6, inlet 2 and outlets 1 and 3 are open. These cases are summarized in Table 2.

Table 2 Different case settings

Case	Inlet	Outlet	Screen
1	1, 2, 3	2	No screen
2	1, 2, 3	2	1
3	1, 2, 3	2	2
4	1, 2, 3	2	1, 2
5	1, 3	2	1, 2
6	2	1, 3	1, 2

2.2 Reaction Model. A laminar flow model is used in this simulation. A species transfer model is used to calculate the mass transfer of MAI and N_2.

The governing equations for fluid flow and energy can be expressed as follows:

Continuity equation:

$$\frac{\partial}{\partial t}(\rho Y_i) + \nabla\cdot(\rho\vec{v}Y_i) = -\nabla\cdot\vec{J}_i + R_i \tag{3}$$

where Y_i is the local mass fraction of each species, R_i is the net rate of production of species i by chemical reaction, and J_i is the diffusion flux of species i, which arises due to gradients of concentration and temperature, as follows:

$$\vec{J}_i = -\rho D_{i,m}\nabla Y_i + D_{T,i}\frac{\nabla T}{T} \tag{4}$$

where $D_{i,m}$ is the mass diffusion coefficient for species i in the mixture and $D_{T,i}$ is the thermal diffusion coefficient.

Momentum equations:

$$\frac{\partial(\rho u)}{\partial t} = -\nabla p + \rho F + \mu\Delta u \tag{5}$$

Energy equation for fluid:

$$\frac{\partial}{\partial t}(\rho E) + \frac{\partial}{\partial x_i}[u_i(\rho E + p)] = \frac{\partial}{\partial x_i}\left(k\frac{\partial T}{\partial x_i} - \sum_i h_i J_i - u_j(\tau_{ij})_{eff}\right) \tag{6}$$

where J_i is the diffusion flux of species i.

A wall surface reaction model is used to calculate the surface deposition process of perovskite. The reaction equation is as follows:

$$CH_3NH_3I + PbI_2 \rightarrow CH_3NH_3PbI_3 \tag{7}$$

Under the operating conditions of the present cell, there is no backward reaction, only forward reaction. The reaction rate constant is defined by the Arrhenius equation:

$$k_{arr} = A_{pre}e^{-E_a/RT} \tag{8}$$

where A_{pre} is the pre-exponential factor, E_a is the activation energy, and R is the gas constant. The activation energy E_a was found to be 110 kJ/mol in Ref. [31]. The pre-exponential constant, A, at our operating conditions is found by measurements, as will be discussed.

In the reaction process, a solid layer of $MAPbI_3$ will grow on the substrates. The MAI vapor must diffuse through the solid layer to react with the PbI_2. To simulate the diffusion process, the diffusion coefficient of MAI vapor through perovskite layer must be found. The diffusion process is schematically shown in Fig. 2. The first step is from face 1 to face 2. The MAI vapor is transferred from the bulk of the gas phase to the gas–solid interface. The mass flux, J_1, in this step is defined as follows:

$$J_1 = h_1\frac{\partial C_{MAI}}{\partial y} \tag{9}$$

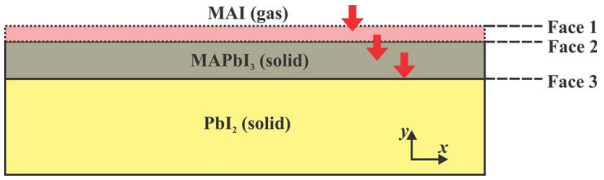

Fig. 2 Diffusion process in the deposition reaction of perovskite

where h_1 is the mass transfer coefficient of MAI vapor and C_{MAI} is the concentration of MAI. The second step is from face 1 to face 2. The MAI vapor diffuses through the perovskite layer to the PbI_2 layer. The mass flux, J_2, in this step is defined as follows:

$$J_2 = D\frac{\partial C_{MAI}}{\partial y} \tag{10}$$

where D is the diffusion coefficient of MAI vapor through the perovskite layer. The third step is on face 3. The MAI reacts with PbI_2 and grows the perovskite layer. The consumption rate of MAI, J_3, in this step is represented as follows:

$$J_3 = kC_{MAI} \tag{11}$$

where k is defined as a reaction constant multiplied by the concentration of PbI_2, $k_{arr}C_{PbI_2}$. The surface concentration of PbI_2 coated on the substrates is C_{PbI_2}. It is estimated from the density and the crystal structure of PbI_2.

As an approximation, we may assume that at steady-state, the bulk concentration of MAI is uniform, and the mass of MAI transferred through the $MAPbI_3$ layer is equal to the mass of MAI consumed by the deposition reaction. By combining Eqs. (9)–(11), we can obtain the following equation:

$$d^2 + \left(\frac{D}{h} + \frac{D}{k}\right)d = \frac{DC_1}{N}t \tag{12}$$

where d is the thickness of the $MAPbI_3$ layer, C_1 is the concentration of MAI at face 1, and t is the reaction time. In this expression, N is the number of MAI molecules incorporated into a unit volume of the $MAPbI_3$ layer, equal to $\rho(MAPbI_3)/M(MAPbI_3)$. If we define as new constants, $A = D/h + D/k$, and $B = DC_1/N$, Eq. (12) can be simplified as follows:

$$d = B\frac{t}{d} - A \tag{13}$$

Therefore, if we measure the thickness of the perovskite layer at several times after the steady-state growth has begun, we can evaluate the values of A and B by fitting the thickness versus time data with Eq. (13) and calculating the diffusion coefficient D.

After finding the value of the diffusion coefficient D, we use it in our numerical simulation. In our simulation, we use a stepwise method to include the effects of the growing thickness of perovskite, as Table 3 presents, realized by the user-defined function. The concentration of MAI at face 2 is C and C^* is the concentration of MAI at face 3, which is calculated by Eqs. (10) and (11). The thickness of the perovskite layer is represented as d. The surface deposition rate of $MAPbI_3$ (SDR) is calculated as follows:

$$\mathrm{SDR} = \frac{kC^*M(\mathrm{MAPbI_3})}{\rho(\mathrm{MAPbI_3})} \tag{14}$$

where M is the molecular weight of $MAPbI_3$. J in Table 3 is the mass flux or mass consumption of MAI. At the beginning of the simulation, $t = t_0$, the thickness of the perovskite layer is 0, and $C = C^*$, and then, J_{t0} and SDR_{t0} can be calculated. After a short time-step, Δt, when $t = t_1$, the thickness of the perovskite layer, d_{t1}, and C^*_{t1} can be calculated based on SDR_{t0} and C_{t1}. Then, the new SDR and J can be calculated. This process proceeds for the successive time-steps.

Table 3 Iteration process to calculate the surface deposition rate of perovskite

t	C	C^*	d	SDR	J
t_0	C_{t0}	$C^*_{t0} = C_0$	$d_{t0} = 0$	SDR_{t0} (Eq. (3))	J_{t0}
t_1	C_{t1}	$C^*_{t1} = DC_1/(kd_1 + D)$	$d_{t1} = d_{t0} + \mathrm{SDR}_{t0}\Delta t$	SDR_{t1}	J_{t1}
			……		

2.3 Fabrication and Thickness Measurement of Perovskite. For evaluation of the diffusion coefficient, D, the thickness of the perovskite films versus time must be measured. The films to be measured are fabricated on a substrate with TiO_2/fluorine-doped tin oxide (FTO)/glass. First, FTO transparent conductive glass substrates (Nippon sheet glass, 14 Ω) are cleaned with the deionized water, ethanol, acetone, and isopropyl alcohol sequentially for 30 min in an ultrasonic bath. Then, about 15 min of oxygen plasma processing is used to chemically remove the organic compounds and other residues from the surfaces of the substrates by the Technics Oxygen Asher. Following this, a TiO_2 film is fabricated on the FTO/glass as soon as possible after the oxygen plasma treatment is completed. The TiO_2 film is deposited twice by spin coating a solution prepared by dissolving 502.5 μL titanium diisopropoxide bis (acetylacetonate) (75 wt% in isopropanol) into 6.35 mL 1-butanol. Each spin coating process is done with a speed of 2000 rpm for 30 s. After each spin coating process, the substrates are baked with a temperature of 140 °C for 10 min before the next step. Then, the substrates are sintered in a CVD tube with a temperature of 550 °C for 60 min. After sintering, the TiO_2 film is cleaned by the oxygen plasma treatment for 5 min. Finally, the perovskite films are deposited on the TiO_2 film substrates. They are fabricated by a hybrid physical–chemical deposition process. First, the PbI_2 film is deposited on the TiO_2/FTO/glass by a spin coating method. A 1.3 M PbI_2/DMF (*N*, *N*-dimethylformamide) solution is spin coated with a speed of 4000 rpm for 30 s. Then, the substrates are baked for 15 min with a temperature of 70 °C. The perovskite film growth process proceeds in a tube furnace (OTF-1200X, MTI Corporation). The substrates, with PbI_2 films, are put into a quartz tube evenly filled with CH_3NH_3I powder (Greatcell Solar Limited), and then, the tube furnace is sealed. When the reaction time has reached the set value, the mechanical pump is opened to end the reaction. During the fabrication process, five samples of PbI_2 perovskite films are prepared. They are as follows: pure PbI_2 (group 0) film, PbI_2 and perovskite films with reaction times of 180 min (group 1), 240 min (group 2), 300 min (group 3), and a pure perovskite film with a reaction time more than 600 min (group 4). In the previous results [32], the PbI_2 film was completely transformed to $CH_3NH_3PbI_3$ film when the reaction time was more than 420 min.

The above processing gives the thickness versus the time data for the perovskite film growth in the environment of the vapor deposition chamber. The process for determining thicknesses is shown in Fig. 3. The thickness of pure PbI_2 film (group 0) is d_0. After all the PbI_2 is transformed to $MAPbI_3$, the thickness of the pure perovskite layer (group 4) is d_4. The thicknesses of the combination of PbI_2 and perovskite film with different reaction times t ($t = 180$, 240, and 300 min) are d_t. When the reaction time is t, the thickness of the growth perovskite layer is $d_{t,\mathrm{MAPbI_3}}$ and the thickness of the unreacted PbI_2 is $d_{t,\mathrm{PbI_2}}$. Then, we have the following equation:

$$d_t = d_{t,\mathrm{MAPbI_3}} + d_{t,\mathrm{PbI_2}} \tag{15}$$

We assume that the ratio of the thickness of the growth of the perovskite layer and the thickness of PbI_2 reacted, d_4/d_0, is constant.

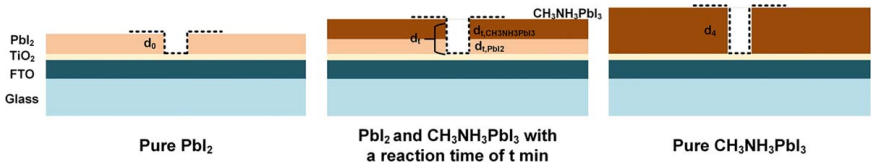

Fig. 3 Schematic diagram of the measurement procedures for determining the thickness of growth of the perovskite layer

Table 4 Thickness of PbI_2 and perovskite films for the five groups

Group	Types of films	Reaction time (min)	Thickness (nm)
0	Pure PbI_2	0	212.70
1	PbI_2 and perovskite film	180	382.68
2	PbI_2 and perovskite film	240	429.21
3	PbI_2 and perovskite film	300	471.70
4	perovskite film	>600	531.09

Table 5 Thickness of growth perovskite layer at different reaction times

Group	Types of films	Reaction time (min)	Thickness of growth perovskite film (nm)
1	PbI_2 and perovskite film	180	283.53
2	PbI_2 and perovskite film	240	361.15
3	PbI_2 and perovskite film	300	432.02

So, at the time t, the thickness of the perovskite layer is equal to the thickness of the reacted PbI_2 multiplied by this ratio. Then, we can have the following equation:

$$d_{t,\mathrm{MAPbI_3}} = (d_0 - d_{t,\mathrm{PbI_2}})\frac{d_4}{d_0} \tag{16}$$

The thicknesses d_0, d_t, and d_4 are measured, and the thickness of the perovskite layer, $d_{t,\mathrm{MAPbI_3}}$, is calculated as follows:

$$d_{t,\mathrm{MAPbI_3}} = d_4\frac{d_4 - d_0}{d_t - d_0} \tag{17}$$

Sharp tweezers are used to remove steps in the five films, and then a surface profile measurement system is used to measure the thicknesses of each of the five films. The measured thicknesses are presented in Table 4. Finally, the thicknesses of the grown perovskite layers are calculated by Eq. (17), and the results are presented in Table 5.

By using Eqs. (12) and (13) and the results presented in Table 5, the constants A and B are found to be 1298 and 41.551, respectively. One thing that should be noticed here is that the value of the two constants will be different if one uses different dimensions or the operating conditions are different. The diffusion coefficient of MAI vapor through the perovskite layer under the operating conditions can be computed through Eq. (13) as 1.58×10^{-11} m^2/s, which is a reasonable value for gas diffusing in solid. The pre-exponential factor A_{pre} is 1.93×10^{16}, which is near the value used by Wang et al. [31], that is, 9×10^{15}. Figure 4(*a*) shows the thickness of the perovskite layer over time as calculated by Eq. (13) using the above values for diffusivity and pre-exponential factor from the experimental measurements. We can see that the experimental points lie on the theoretical model curve perfectly. Figure 4(*b*) shows the growth of thickness of the perovskite layer over time calculated by Eq. (13) and by numerical simulation. They agree well. We also tried to directly fit the experimental points with our numerical simulation. The value of the diffusion coefficient backed out from that analysis is 1.3×10^{-11}. It is suitably close to the value computed from the analytical model presented earlier. The difference may come from the following: (1) the pressure and concentration calculated by the numerical simulation may be slightly different from that we used in the theoretical model; (2) the mass transfer coefficient in the gas phase calculated by numerical simulation may be different from that we used in the theoretical model; and (3) there may be errors caused by the calculation method in the numerical simulation.

3 Results and Discussion

Figure 5 shows the average surface deposition rate and thickness of $MAPbI_3$ layer on the substrates over time for all the cases. For each case, the surface deposition rate first increases and then

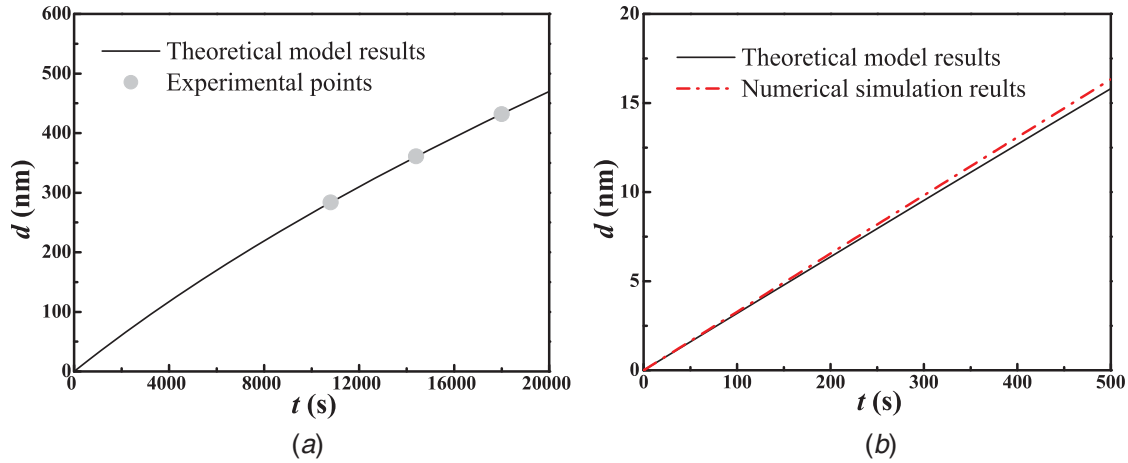

Fig. 4 Comparison of the growth of thickness over time: (*a*) theoretical and experimental results and (*b*) theoretical and numerical results

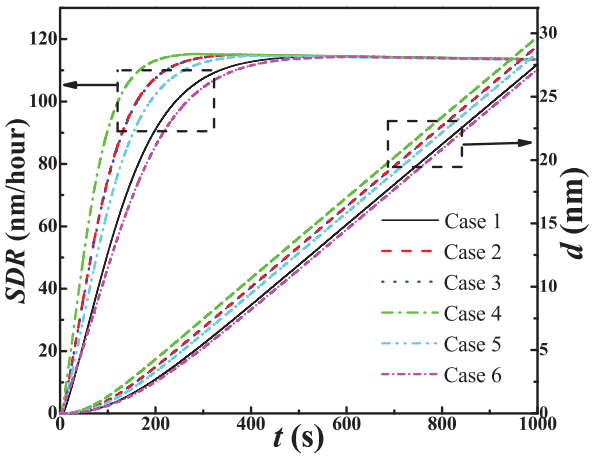

Fig. 5 Averaged surface deposition rate and thickness of $MAPbI_3$ layer on the substrate over time for cases 1–6

becomes more stable with a mild drop. That is because at the beginning of the simulation, the reaction plenum is filled with N_2, and MAI vapor is introduced through the inlets. With time, more MAI molecules reach the substrates and react with the PbI_2 on the surface. The molecular concentration of MAI on the substrate surface increases with time, leading to the increasing surface deposition rate. After the N_2 becomes purged from the plenum, the rate of MAI concentration on the surface decreases and finally becomes stable. This is the point when the concentration of MAI for surface deposition becomes stable. However, with the continuing of the reaction, the thickness of the perovskite layer increases and the surface deposition rate decreases since the MAI molecules must diffuse through the perovskite layer to react with the PbI_2. Therefore, the surface deposition rate drops regularly with time after all the N_2 is purged. Comparing cases 1–4, we can see that the surface deposition of case 4 increases most rapidly, and case 1 increases most slowly. Cases 2 and 3 have almost the same surface deposition rate. Therefore, the thickness of case 4 is larger than those of cases 1–3 during the period simulated (1000 s). This leads to a lower surface deposition rate of case 1 after the molecular concentration of MAI becomes stable in the plenum, which is hard to see in Fig. 6 as the thickness differences are small. The turning point of the SDR curve for case 4 appears earlier than for cases 2 and 3, and the turning points of the SDR curves for cases 2 and 3 appear earlier than for case 1, which means that case 1 can purge the N_2 from the plenum more quickly than cases 2 and 3 can, and cases 2 and 3 can purge the N_2 from the plenum quicker than case 1 can. Comparing cases 4–6, we can see that the surface deposition of case 4 increases the fastest, and case 6 increases the slowest. This is because case 4 has three MAI inlets, while case 5 has two MAI inlets and case 6 has one MAI inlet. Case 4 has higher mass flowrate of MAI than cases 5 and 6, and therefore, case 4 has a higher surface deposition rate at the times before the N_2 is purged. Also, we can see that the turning point of the SDR curve for case 5 appears earlier than that for case 1, which means that adding screens can help purge the N_2 and the consumption of MAI is reduced.

Figure 6 shows the surface deposition rate distributions on the left substrate for cases 1–6 at 80 s and 320 s. When $t = 80$ s, a comparison of cases 1–4, we can see that case 4 has the highest surface deposition rate, while case 1 has the lowest. Cases 2 and 3 have similar surface deposition rates. This shows that adding screens helps in purging the N_2 more quickly and brings more MAI to the substrate. Comparing cases 4–6, we can see that case 4 has the highest surface deposition rate and case 6 has the lowest. For case 5, the surface deposition rate on the left is higher than that on the right, while for case 6, the surface deposition rate on the right is higher than that on the left. This is because case 5 has inlets 1 and 3 open, and case 6 has only inlet 2 open. The left side of the substrate of case 5 is closer to the MAI inlet, while the right side of the substrate of case 6 is closer to the MAI inlet. This means that the MAI vapor flow is highly influenced by the geometry. When $t = 320$ s, most of the N_2 has already been purged, and the differences in the surface deposition rate between different cases become smaller. All the cases, including cases 5 and 6, show a uniform distribution of the surface deposition rate on the substrate.

To analyze the uniformity of the surface deposition rate on the substrate, we define a new parameter called surface deposition rate deviation to show the deviation of the local surface deposition rate (SDR) from the averaged value ($\overline{\text{SDR}}$), as follows:

$$\text{SDRD} = \frac{\text{SDR} - \overline{\text{SDR}}}{\overline{\text{SDR}}} \tag{18}$$

Figure 7 shows the surface deposition rate deviations on the left substrate for cases 1–6 at 80 s and 320 s. When $t = 80$ s, comparing cases 1–4, we can see that case 4 has the most uniform surface deposition rate distribution. Cases 2 and 3 have similar uniformity. Case 1 is the least uniform. Comparing cases 4–6, we can see that cases 5 and 6 have poor uniformity of the surface deposition rate, because the molecular concentration of MAI is higher near the mass flow inlets. When $t = 320$ s, the surface deposition rate deviation becomes very small for all the cases, as most of N_2 has been purged out.

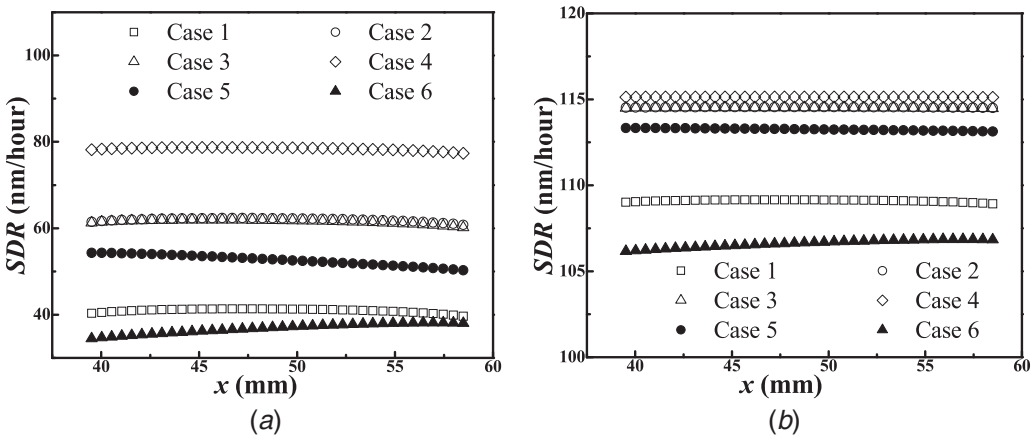

Fig. 6 Surface deposition rate distributions on the left substrate for cases 1–6 at (*a*) $t = 80$ s and (*b*) $t = 320$ s

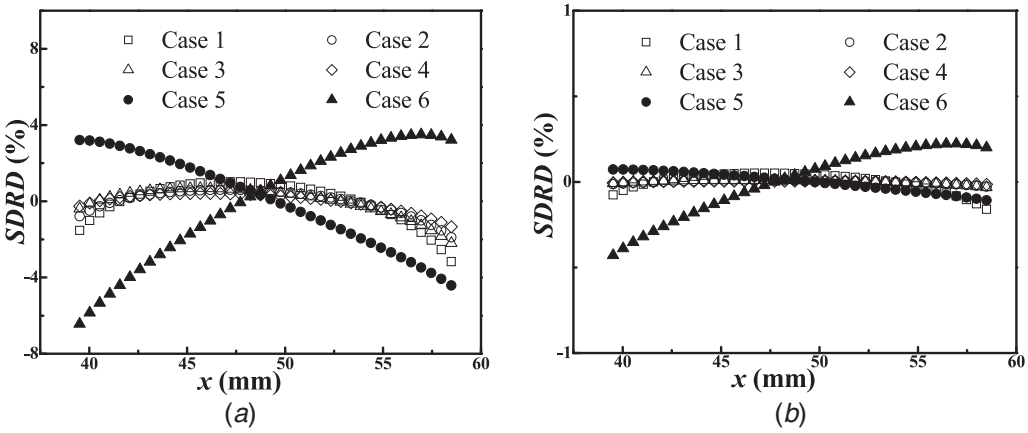

Fig. 7 Surface deposition rate deviations on the left substrate for cases 1–6 at (*a*) $t = 80$ s and (*b*) $t = 320$ s

Figure 8 shows contours of pressure and streamlines for cases 1–6 at $t = 80$ s. From cases 1–4, we can see the influence of adding screens. For case 2, there is a pressure drop on the upper screen (screen 1), and the streamlines of MAI are forced to distribute more uniformly across the screen, especially for the MAI from the middle inlet (inlet 2). The distribution of the streamlines below the screen is also influenced. For case 3, the pressure drop occurs on the lower screen (screen 2), and the distribution of streamlines is more uniform above the screen, compared with case 1, especially for the MAI from the inlets on the left and right (inlets 1 and 3).

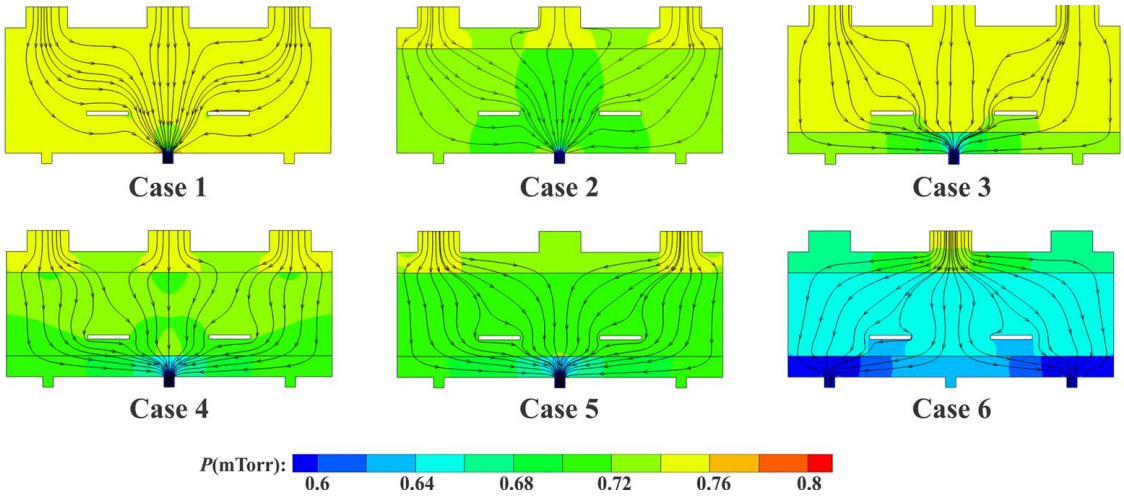

Fig. 8 Contours of pressure and streamlines for cases 1–6 at $t = 80$ s

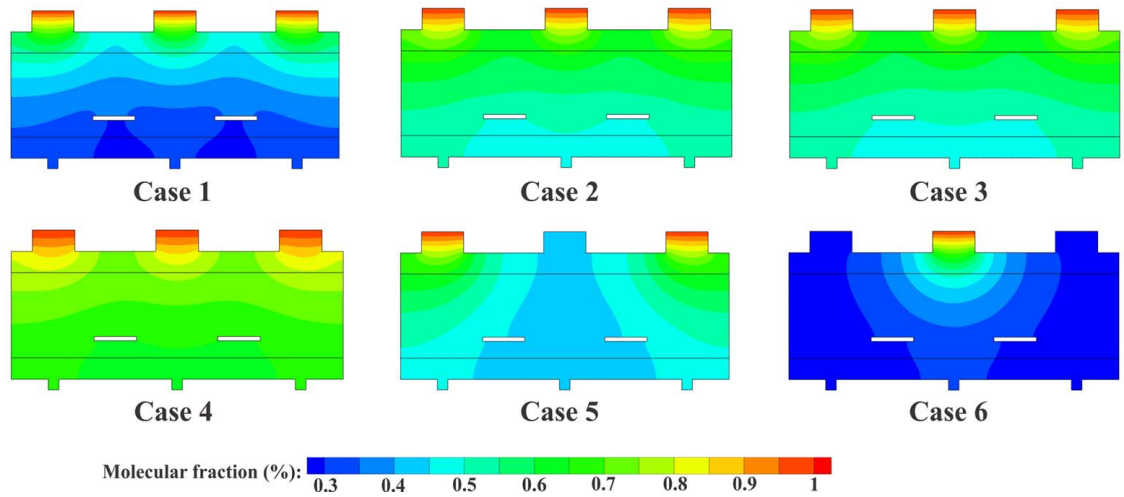

Fig. 9 Contours of molecular fraction of MAI for cases 1–6 at $t = 80$ s

After adding both screens, like case 4, we can see that the streamlines between the two screens are more uniform than in cases 1–3, which will make the MAI concentration distribution on the substrate more uniform. This explains why case 4 has a more uniform surface deposition rate than other cases. As for cases 5 and 6, the distribution of MAI concentration on the substrates is not as uniform as in cases 1–4, but we can see that most of the streamlines will pass the substrates, while for cases 1–4, most of the MAI from the middle inlet flows directly out through the middle outlet. This explains why cases 5 and 6 have more than 2/3 and 1/3 of the surface deposition rate, respectively, with only 2/3 and 1/3 of the mass flowrate of case 4.

Figure 9 shows contours of mole fraction of MAI for cases 1–6 at $t = 80$ s. Comparing cases 1–4, we can see that case 4 has the highest mole fraction of MAI, while case 1 has the lowest, and cases 2 and 3 have similar mole fraction values. This explains why case 4 has a higher surface deposition rate than the other cases at the same time. This is due to the screens that make the MAI vapor flow more uniform in the plenum, and then, the N_2 near the wall and in the corner can be mixed with MAI vapor and purged out more efficiently than in case 1 (without screens). Case 5 has a lower mole fraction of MAI in the middle part, while case 6 has a higher mole fraction of MAI in the middle part. Therefore, on the left substrate, the surface deposition rate of case 5 increases from left to right, while the surface deposition rate of case 6 decreases from left to right, as shown in Fig. 6(*a*).

4 Conclusions

A numerical model is established to simulate the vapor deposition process in the fabrication of a perovskite solar cell. The diffusion process of MAI vapor through the growing perovskite layer is part of the analysis. It employs a diffusion coefficient calculated from measurements of the growth of a perovskite layer in a deposition cell that is the same as the one analyzed. To the authors' knowledge, this is the first evaluation of diffusivity of MAI through the perovskite used herein. The simulation of the vapor deposition chamber is used to improve the deposition process. One feature is the use of screens. Their influence when positioned at various locations in the plenum is analyzed. The influences of inlets and outlets, numbers, and locations, are also quantified. The following conclusions are presented:

(1) In the vapor deposition process of a perovskite solar cell, the overall surface deposition rate will first increase, as the MAI concentration increases in the plenum. After N_2 is purged, the MAI concentration becomes stable within the plenum, but the surface deposition rate will decline with time because of the increasing thickness of the perovskite layer making the diffusion process slow.
(2) Adding screens makes the MAI vapor flow more uniform in the plenum and quickens the purge rate of N_2 precursor gas, leading to higher and more uniform surface deposition rate in the early part of the vapor deposition process.
(3) The flow of MAI vapor has a very low Reynolds number, and the flow is highly influenced by the geometry. Therefore, the effects of geometry of the reaction plenum, including the number and locations of MAI inlets, substrates, and outlets should be well understood toward achieving a design that gives a uniform and controlled surface deposition rate of the perovskite layer.

Acknowledgment

A portion of this work was supported by the China Scholarship Council (CSC). The numerical part of this work was carried out using computing resources at the University of Minnesota Supercomputing Institute.

Data Availability Statement

The datasets generated and supporting the findings of this article are obtainable from the corresponding author upon reasonable request. The authors attest that all data for this study are included in the paper. Data provided by a third party listed in Acknowledgments. No data, models, or code were generated or used for this paper.

References

[1] Akihiro, K., Kenjiro, T., Yasuo, S., and Tsutomu, M., 2009, "Organometal Halide Perovskites as Visible-Light Sensitizers for Photovoltaic Cells," J. Am. Chem. Soc., **131**(17), pp. 6050–6051.
[2] The National Renewable Energy Laboratory (NREL), 2019, https://www.nrel.gov/pv/assets/pdfs/best-research-cell-efficiencies.20190802.pdf
[3] Wojciechowski, K., Saliba, M., Leijtens, T., Abate, A., and Snaith, H. J., 2014, "Sub-150 °C Processed Meso-Superstructured Perovskite Solar Cells With Enhanced Efficiency," Energy Environ. Sci., **7**(3), pp. 1142–1147.
[4] Ray, R., Sarker, A. S., and Pal, S. K., 2019, "Improving Performance and Moisture Stability of Perovskite Solar Cells Through Interface Engineering With Polymer-2D MoS_2 Nanohybrid," Sol. Energy, **193**, pp. 95–101.
[5] Wang, J. T., Ball, J. M., Barea, E. M., Abate, A., Alexander-Webber, J. A., Huang, J., Saliba, M., Mora-Sero, I., Bisquert, J., Snaith, H. J., and Nicholas, R. J., 2013, "Low-Temperature Processed Electron Collection Layers of Graphene/TiO_2 Nanocomposites in Thin Film Perovskite Solar Cells," Nano Lett., **14**(2), pp. 724–730.
[6] Duan, J., Wu, J., Zhang, J., Xu, Y., and Lund, P. D., 2016, "TiO_2/ZnO/TiO_2 Sandwich Multilayer Films as a Hole-Blocking Layer for Efficient Perovskite Solar Cells," Int. J. Energy Res., **40**(6), pp. 806–813.
[7] Yang, L., Yang, P., Wang, J., Hao, Y., Li, Y., Lin, H., and Zhao, X., 2019, "Low-Temperature Preparation of Crystallized Graphite Nanofibers for High Performance Perovskite Solar Cells," Sol. Energy, **193**, pp. 205–211.
[8] Ying, C., Shi, C., Wu, N., Zhang, J., and Wang, M., 2015, "A Two-Layer Structured pbi2 Thin Film for Efficient Planar Perovskite Solar Cells," Nanoscale, **7**(28), pp. 12092–12095.
[9] Li, Y. B., Cooper, J. K., Buonsanti, R., Giannini, C., Liu, Y., Toma, F. M., and Sharp, I. D., 2015, "Fabrication of Planar Heterojunction Perovskite Solar Cells by Controlled Low-Pressure Vapor Annealing," J. Phys. Chem. Lett., **6**(3), pp. 493–499.
[10] Subbiah, A. S., Halder, A., Ghosh, S., Mahuli, N., Hodes, G., and Sarkar, S. K., 2014, "Inorganic Hole Conducting Layers for Perovskite-Based Solar Cells," J. Phys. Chem. Lett., **5**(10), pp. 1748–1753.
[11] Kim, B. S., Kim, T. M., Choi, M. S., Shim, H. S., and Kim, J. J., 2015, "Fully Vacuum–Processed Perovskite Solar Cells With High Open Circuit Voltage Using MoO_3/NPB as Hole Extraction Layers," Org. Electron., **17**, pp. 102–106.
[12] Zhao, D., Ke, W., Grice, C. R., Cimaroli, A. J., Tan, X., Yang, M., Collins, R. W., Zhang, H., Zhu, K., and Yan, Y., 2015, "Annealing-Free Efficient Vacuum-Deposited Planar Perovskite Solar Cells With Evaporated Fullerenes as Electron-Selective Layers," Nano Energy, **19**, pp. 88–97.
[13] Chen, Q., Zhou, H., Hong, Z., Luo, S., Duan, H. S., Wang, H. H., Liu, Y., Li, G., and Yang, Y., 2014, "Planar Heterojunction Perovskite Solar Cells via Vapor-Assisted Solution Process," J. Am. Chem. Soc., **136**(2), pp. 622–625.
[14] Chen, Q., Zhou, H., Song, T. B., Luo, S., Hong, Z., Duan, H. S., Dou, L., Liu, Y., and Yang, Y., 2014, "Controllable Self-Induced Passivation of Hybrid Lead Iodide Perovskites Toward High Performance Solar Cells," Nano Lett., **14**(7), pp. 4158–4163.
[15] Zhou, H., Chen, Q., and Yang, Y., 2015, "Vapor-Assisted Solution Process for Perovskite Materials and Solar Cells," MRS Bull., **40**(8), pp. 667–673.
[16] Wang, S., Ono, L. K., Leyden, M. R., Kato, Y., Raga, S. R., Lee, M. V., and Qi, Y. B., 2015, "Smooth Perovskite Thin Films and Efficient Perovskite Solar Cells Prepared by the Hybrid Deposition Method," J. Mater. Chem. A, **3**(28), pp. 14631–14641.
[17] Leyden, M. R., Ono, L. K., Raga, S. R., Kato, Y., Wang, S., and Qi, Y., 2014, "High Performance Perovskite Solar Cells by Hybrid Chemical Vapor Deposition," J. Mater. Chem. A, **2**(44), pp. 18742–18745.
[18] Leyden, M. R., Lee, M. V., Raga, S. R., and Qi, Y. B., 2015, "Large Formamidinium Lead Trihalide Perovskite Solar Cells Using Chemical Vapor Deposition With High Reproducibility and Tunable Chlorine Concentrations," J. Mater. Chem. A, **3**(31), pp. 16097–16103.
[19] Peng, Y., Jing, G., and Cui, T., 2015, "A Hybrid Physical-Chemical Deposition Process at Ultra-Low Temperatures for High-Performance Perovskite," J. Mater. Chem. A, **3**(23), pp. 12436–12442.
[20] Wehrenfennig, C., Liu, M., Snaith, H. J., Johnston, M. B., and Herz, L. M., 2014, "Charge-Carrier Dynamics in Vapour-Deposited Films of the Organolead Halide Perovskite $CH_3NH_3PbI_{3-x}Cl_x$," Energy Environ. Sci., **7**(7), pp. 2269–2275.
[21] Jeon, N. J., Noh, J. H., Kim, Y. C., Yang, W. S., Ryu, S., and Seok, S. I., 2014, "Solvent Engineering for High-Performance Inorganic–Organic Hybrid Perovskite Solar Cells," Nat. Mater., **13**(9), pp. 897–903.
[22] Agrafiotis, C., Pein, M., Giasafaki, D., Tescari, S., Roeb, M., and Sattler, C., 2019, "Redox Oxides-Based Solar Thermochemistry and Its Materialization to Reactor/Heat Exchanger Concepts for Efficient Solar Energy Harvesting, Transformation and Storage," ASME J. Sol. Energy Eng., **141**(2), p. 021010.

[23] Udayabhaskararao, T., Kazes, M., Houben, L., Lin, H., and Oron, D., 2017, "Nucleation, Growth, and Structural Transformations of Perovskite Nanocrystals," Chem. Mater., **29**(3), pp. 1302–1308.
[24] Xue, H., Bergirsson, E., and Stangl, R., 2019, "Correlating Variability of Modeling Parameters With Photovoltaic Performance: Monte Carlo Simulation of a Meso-Structured Perovskite Solar Cell," Appl. Energy, **237**, pp. 131–144.
[25] Yang, C., Simon, T., and Cui, T., 2017, "Numerical Simulation and Analysis of Hybrid Physical-Chemical Vapor Deposition to Grow Uniform Perovskite $MAPbI_3$," J. Appl. Phys., **121**(14), pp. 1989–1997.
[26] Arivazhagan, V., Xie, J., Yang, Z., Hanga, P., Parvathia, M. M., Xiao, K., Cui, C., Yang, D., and Yu, X., 2019, "Vacuum Co-Deposited $CH_3NH_3PbI_3$ Films by Controlling Vapor Pressure for Efficient Planar Perovskite Solar Cells," Sol. Energy, **181**, pp. 339–344.
[27] Joback, K. G., and Reid, R. C., 1987, "Estimation of Pure-Component Properties From Group-Contributions," Chem. Eng. Commun., **57**(1), pp. 233–243.
[28] Curtiss, C. F., Hirschfelder, J. O., and Bird, R. B., 1954, *Molecular Theory of Gases and Liquids*, John Wiley & Sons, New York.
[29] Onoda-Yamamuro, N., Matsuo, T., and Suga, H., 1992, "Dielectric Study of $CH_3NH_3Pbx_3$ (x = Cl, Br, I)," J. Phys. Chem. Solids, **53**(7), pp. 935–939.
[30] Idel'chik, I. E., and Steinberg, M. O., 1996, *Handbook of Hydraulic Resistance*, 4th ed., Begell House, New York.
[31] Wang, B., Young Wong, K., Xiao, X., and Chen, T., 2015, "Elucidating the Reaction Pathways in the Synthesis of Organolead Trihalide Perovskite for High-Performance Solar Cells," Sci. Rep., **5**(1), p. 10557.
[32] Wei, X., Peng, Y., Jing, G., and Cui, T., 2018, "Planar Structured Perovskite Solar Cells by Hybrid Physical Chemical Vapor Deposition With Optimized Perovskite Film Thickness," Jpn. J. Appl. Phys., **57**(5), p. 052301.

Xiangyang Wei
State Key Laboratory of Precision Measurement Technology and Instruments, Department of Precision Instrument, Tsinghua University, Beijing 100084, China
e-mail: wei-xy14@mails.tsinghua.edu.cn

Yanke Peng
State Key Laboratory of Precision Measurement Technology and Instruments, Department of Precision Instrument, Tsinghua University, Beijing 100084, China
e-mail: pengyk@mail.tsinghua.edu.cn

Gaoshan Jing
State Key Laboratory of Precision Measurement Technology and Instruments, Department of Precision Instrument, Tsinghua University, Beijing 100084, China
e-mail: jinggaoshan@ime.ac.cn

Terrence Simon
Department of Mechanical Engineering, University of Minnesota, Minneapolis, MN 55455
e-mail: simon002@umn.edu

Tianhong Cui[1]
Department of Mechanical Engineering, University of Minnesota, Minneapolis, MN 55455
e-mail: tcui@me.umn.edu

High-Performance Perovskite Solar Cells Fabricated by a Hybrid Physical–Chemical Vapor Deposition

For the first time, we used a hybrid physical–chemical vapor deposition (HPCVD) method to fabricate perovskite solar cells (PSCs) based on perovskite films with both organic cations and halogen anions. A high power conversion efficiency (PCE) of 18.1% was achieved based on a mixed perovskite film of $MA_xFA_{1-x}Pb\ (I_yBr_{1-y})_3$ and the efficiency of the PSCs with $MAPbI_3$ and $MA_xFA_{1-x}PbI_3$ films were 14.5% and 16.4%, respectively. Perovskite material components and bandgaps were precisely tuned to achieve high photoelectric conversion performance. Three different types of perovskite films employed include $MAPbI_3$, $MA_xFA_{1-x}PbI_3$, and $MA_xFA_{1-x}Pb\ (I_yBr_{1-y})_3$ (which are also designated as $MAPbI_3$, $MA_{0.89}FA_{0.11}PbI_3$, and $MA_{0.54}FA_{0.46}Pb\ (I_{0.94}Br_{0.06})_3$ with the respective bandgaps of 1.60 eV, 1.58 eV, and 1.61 eV. The experimental results demonstrate the ability to fabricate both organic cation and halogen anion mixed perovskite films by the HPCVD method and achieve easily adjustable bandgaps. In addition, the perovskite films fabricated by HPCVD have superior surface morphology, large crystal size, and low surface roughness. Eventually, this vapor-based method will have great potential in the fabrication of large-area and flexible PSCs to promote commercial application and industrialization of future PSCs. [DOI: 10.1115/1.4049326]

Keywords: perovskite solar cells, hybrid physical–chemical vapor deposition, mixed perovskite films, adjustable bandgap, energy, photovoltaics, solar

Introduction

In the last decade, solar cells based on inorganic–organic perovskite material have attracted significant research interest as a promising renewable energy technology [1]. The power conversion efficiency (PCE) of the perovskite solar cells (PSCs) has surged from 3.8% [2] to 25.2% [1] since it was first reported in 2009 [2]. The certificated PCE of PSCs has improved more than any other types of single junction solar cells, such as the CIGS (23.4%), CdTe (22.1%), and the multi-crystalline silicon solar cells (22.3%) [1]. Only the single crystal silicon solar cells (26.1%) and single crystal GaAs solar cells (27.8%) boast higher PCEs [1]. To broaden the PSCs applications in the future, it is critical to develop fabrication methods for high-performance PSCs that can be manufactured at a high deposition rate.

Compared with other commercially available inorganic solar cells, one of the excellent properties of hybrid inorganic–organic perovskite is that its components can be tuned in a larger number of ways. Superior performance can be easily achieved just by modifying organic cations or halogen anion components. A typical perovskite's formula is AMX_3, in which A represents the organic cation such as methylammonium (MA, CH_3NH_3I) and formamidinium (FA, $CH(NH_2)_2$), M represents the metal cation such as lead (Pb) and tin (Sn), and X represents the halogen anion including chlorine (Cl), bromine (Br), and iodine (I) [3]. For example, compared with the intensively investigated $MAPbI_3$, mixed perovskite films ($MA_xFA_{1-x}Pb\ (I_yBr_{1-y})_3$) can be synthesized by mixing organic cations and halogen anion components. Theoretically, the optimal bandgap of the light absorption film for solar cells is about 1.4 eV at which the highest PCE could be achieved is 33% [4]. However, the bandgap of $MAPbI_3$ is about 1.57 eV, which is much larger than the optimal bandgap of 1.4 eV. Larger bandgap can lead to narrower wavelength light absorption [5,6]. By modifying the perovskite material's components, the perovskite film's bandgap can be readily adjusted. For the $MA_xFA_{1-x}Pb\ (I_yBr_{1-y})_3$ film, a wide bandgap in the 1.48–2.23 eV range can be achieved by tuning the percentage of organic cations and halogen anions [5]. Up to now, most of the PSCs reported with PCE values larger than 20% are based on mixed perovskite layers [7–11]. Additionally, the performance of PSCs with mixed perovskite films containing the FA group show improved thermal stability and crystal phase stability with lower hysteresis [12–14]. Furthermore, surface morphology can be improved, and the defects can be reduced by introducing Br^- into the perovskite film [12,15,16]. Zhu's group shows that $MAPbI_3$ films with some Br incorporation have large crystals with micrometer size, and no pinholes [16]. By using admittance spectroscopy, Yang et al. showed that Br^- ions introduced into perovskite material to partially replace I^- ions can decrease trap state densities to improve PSCs' performance [15].

The quality of perovskite films is a critical factor in determining the efficiency of PSCs, which is greatly affected by the fabrication methods used to synthesize perovskite films [17,18]. Fabrication methods for perovskite films can be categorized into two groups: solution-based methods ("wet") [19,20] and vapor-based methods

[1]Corresponding author.

Contributed by the Solar Energy Division of ASME for publication in the JOURNAL OF SOLAR ENERGY ENGINEERING: INCLUDING WIND ENERGY AND BUILDING ENERGY CONSERVATION. Manuscript received May 7, 2020; final manuscript received November 26, 2020; published online January 12, 2021. Editor: S.A. Sherif.

("dry") [21–23]. In certain cases, solution-based methods can also be applied in a few steps or in combination with vapor-based methods to synthesize perovskite films [24,25]. Currently, the solution-based method to synthesize perovskite films has the following apparent advantages: low cost and a modest requirement for fabrication facility [17,26]. Various modified solution methods have been developed to precisely control the crystalline process and nearly all the PSCs with PCE over 20% are fabricated by these methods [27–29]. For instance, vapor or antisolvent is used in the spin coating process to increase the crystalline process while increasing evaporation of solution. Jeon et al. were first reported to use the antisolvent method to fabricate extremely uniform and dense perovskite layers [30]. By this method, the PSCs based on the above perovskite layer also obtained a high efficiency of 16.2%. By optimizing the whole spin coating process using antisolvent, Singh and Miyasaka obtained PSCs with reproducible PCEs up to 20.8% [31]. The fabrication process of the solution-based methods that can achieve high efficiency is still quite complex, as reported in the abovementioned published paper. In addition, various process parameters must be precisely controlled to promote their application in the fabrication of large-area solar cells with industrial production.

Though vapor-based methods are not as widely used as solution-based methods, several vapor-based methods have been thoroughly investigated. The first reported method used the dual source evaporation method, which was introduced by Liu et al. [21]. Two precursors, including CH_3NH_3I and $PbCl_2$, were evaporated at the same time to react into the perovskite film within dual source evaporation equipment. By this method, a higher efficiency of 15.4% was achieved. Additionally, the vapor-assistant solution process [23] and hybrid chemical vapor deposition [32] were developed for the synthesis of perovskite films. In our previously published papers, we developed a hybrid physical–chemical vapor deposition method (HPCVD) to fabricate high-quality and uniform $CH_3NH_3PbI_3$ films [33]. Meanwhile, the detailed working mechanisms were thoroughly investigated [33,34]. The fabricated $CH_3NH_3PbI_3$ films were of high quality at a fabrication temperature of only 73 °C [33]. The resulting PSCs achieved a high PCE of up to 14.7% and were highly stable. In a subsequent work, the HPCVD process parameters, such as growth temperature, vapor pressure, vapor atmosphere, and the guiding airflow in the HPCVD process were precisely controlled [18]. The fabricated PSCs based on $CH_3NH_3PbI_3$ films achieved a higher PCE up to 15.5%. Several research groups have since used vapor-based methods to fabricate mixed perovskite films. Chen et al. introduced a low-pressure, vapor-assisted solution process to fabricate $FA_xMA_{1-x}PbI_3$ based PSCs [35]. The $FA_xMA_{1-x}PbI_3$ films were obtained by mixing a series of MAI and FAI powders with different mass ratios in the CVD process. Subsequently, a high efficiency of 16.48% was achieved when the mass ratio of MAI to FAI was 4:6 [35]. Jiang et al. demonstrated a way to fabricate PSCs based on a $Cs_xFA_{1-x}PbI_3$ film. A solution-assisted vapor method and cation exchange method were combined in their work [36]. The $FAPbI_3$ films were initially fabricated by a solution-assisted vapor method and then immersed in a $CsCH_3COO$/IPA solution to get the $Cs_xFA_{1-x}PbI_3$ film. A high PCE of 15.0% was achieved by this method. Zhu et al. used a vacuum co-evaporation deposition method to deposit $PbCl_2$ and CsCl at the same time in the first step [37]. Then, the $PbCl_2$ and CsCl film were placed on a layer of MAI powder heated to 150 °C for 20 min. By this method, the fabricated PSCs obtained a high PCE of 20.13% [37]. Thus far, mixed perovskite films with halogen anions fabricated by the vapor-based method have not been reported.

In this paper, for the first time, a vapor-based method is used to fabricate mixed PSCs based on both organic cations and halogen anions. The components and bandgaps of perovskite materials fabricated by the HPCVD method are precisely adjusted to achieve high photoelectric conversion performance. The three types of fabricated perovskite material can be described as $MAPbI_3$, $MA_{0.89}FA_{0.11}PbI_3$, and $MA_{0.54}FA_{0.46}Pb(I_{0.94}Br_{0.06})_3$. The bandgap of the three kinds of perovskite material are 1.60 eV, 1.58 eV, and 1.61 eV, respectively. The PCEs of the PSCs based on the three types of perovskite films ($MA_xFA_{1-x}Pb(I_yBr_{1-y})_3$, $MA_xFA_{1-x}PbI_3$, and $MAPbI_3$) are 18.1%, 16.4%, and 14.5%, respectively. The experimental results demonstrate the feasibility of fabricating both organic cation and halogen anion mixed perovskite films by the HPCVD method. Adjustable components and bandgaps of the mixed $MA_xFA_{1-x}Pb(I_yBr_{1-y})_3$ films can be easily achieved. Ultimately, this vapor-based method has great potential for fabrication of large-area and flexible PSCs. It will help to promote the commercial application and industrialization of future PSCs.

Experimental Methods

The fabricated PSCs are composed of a planar structure of glass/FTO/TiO_2/perovskite film/Spiro-OMeTAD/Au. The cross-sectional SEM image of the perovskite solar cell based on $MAPbI_3$ film is shown in Fig. 1(*a*). A three-dimensional schematic of the perovskite solar cell device architecture is shown in Fig. 1(*b*), including the patterns of the gold electrode and etched FTO. The treatment for FTO glass and the fabrication process for TiO_2 are the same as in our previous work [18]. The difference is the fabrication process of the perovskite films. The perovskite films are $MAPbI_3$, $MA_xFA_{1-x}PbI_3$, and $MA_xFA_{1-x}Pb(I_yBr_{1-y})_3$ for different types of PSCs. Details of the fabrication process by the HPCVD

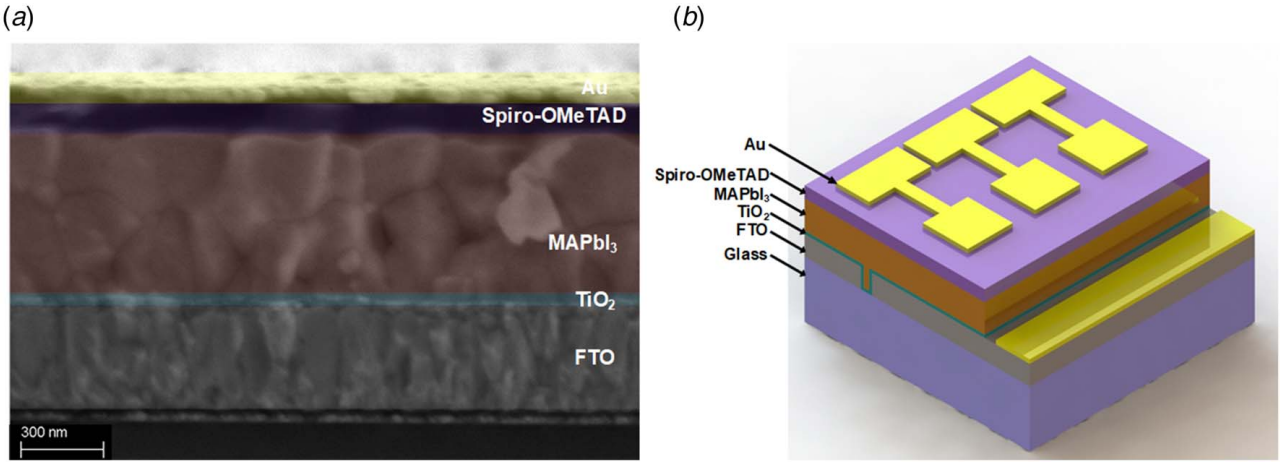

Fig. 1 (*a*) Cross-sectional SEM image and (*b*) schematic device architecture of the perovskite solar cells with a planar structure of FTO/TiO_2/$MAPbI_3$/Spiro-OMeTAD/Au

method are shown in Fig. 2. In the fabrication process of a perovskite film, a PbI_2 film was first deposited on the TiO_2/FTO/glass substrates by spin coating a 1.3 mol/l PbI_2 precursor solution. For the precursor solution, PbI_2 powder was completely dissolved into a mixed solution of N,N-dimethylformamide (DMF, Sigma) and dimethyl sulfoxide (DMSO, Sigma). The volume ratio of DMF to DMSO was 95%:5%. The spin coating process is shown in the left of Fig. 2(*a*). A speed of 2500 rpm was applied for 60 s. Next, the PbI_2 films were annealed for 60 s at a temperature of 70 °C, as shown in the right of Fig. 2(*a*). The growth process of perovskite material is different for different types of perovskite films. For the $MAPbI_3$ film shown in Fig. 2(*b*), the PbI_2 films and MAI powder were put into the CVD tube. The reaction time and growth temperature were set at 420 min and 110 °C. For the $MA_xFA_{1-x}PbI_3$ film shown in Fig. 2(*c*), the PbI_2 substrates were combined with MAI and FAI mixed powders with a mass ratio of 0.5:0.5 and were put into the CVD tube. The reaction time and growth temperature were set at 30 min and 160 °C. Lastly, for the $MA_xFA_{1-x}Pb\ (I_yBr_{1-y})_3$ film shown in Fig. 2(*d*), the PbI_2 films were combined with MABr and FAI powder with a mass ratio of 0.05: 0.95 and were put into the CVD tube. The reaction time and growth temperature were set at 420 min and 115 °C. In the CVD process, the tube was first pumped down to 20 mTorr by running a mechanical pump during the preheating process. When the temperature came to the set growth temperature, the mechanical pump was shut down to make sure that the evaporated MAI, MABr, or FAI vapor reacted with the whole PbI_2 film. Then, a Spiro-OMeTAD (Lumtech, Taiwan) film was coated on the perovskite film by spin coating at 6000 rpm as our previous work [18]. Finally, a thermal evaporation (SKY Technology Development Co. Ltd., Chinese Academy of Science, China) was used to deposit a gold layer 70 nm thick on the Spiro-OMeTAD film as the electrode. For the first 10 nm, the evaporated rate was 0.2 Å/s, and then was 0.8 Å/s for the next 60 nm. The patterns of the gold electrode were formed by using a stainless steel shadow mask in the evaporation process.

Surface morphology of perovskite films was characterized by a field-emission scanning electron microscope (FE-SEM, Zeiss Merlin, Germany). The crystalline phase and structure were characterized by X-ray diffraction (XRD) equipment. The X-ray photoelectron spectroscopy (XPS) spectrum of the three different types of perovskite films were characterized by PHI Quantera II. A UV/Vis Spectrophotometer (LAMBDA 950, PerkinElmer) was used to measure the absorption spectrum of the three types of perovskite films. An atomic force microscope (MFP-3D OriginTM, Oxford Instrument) was used to characterize the surface morphology and measure the surface roughness of the PbI_2 and perovskite films. The current density–voltage (J-V) curves were measured by a semiconductor Device Parameter Analyzer (B1500A, Keysight, Santa Rosa, CA). AM 1.5 illumination light was provided by a Newport ABB (94021A, Irvine, CA) solar simulator. A mono-silicon reference cell (Newport calibration cert, #0702, Irvine, CA) was used to calibrate the intensity of the illumination light. A stainless steel mask with an area of 9 mm^2 was used to measure the real active area of the PSCs. The voltage scanning parameters were set from −0.1 V to 1.2 V, with a step of 50 mV and a delay time of 50 ms.

Results and Discussion

In this work, we successfully fabricated two kinds of mixed perovskite films, $MA_xFA_{1-x}PbI_3$ and $MA_xFA_{1-x}Pb\ (I_yBr_{1-y})_3$, by using the HPCVD method for the first time. Simultaneously, we fabricated an $MAPbI_3$ film for comparison. For mixed perovskite films fabricated by solution-based methods, the element ratio of the film can be calculated by the ratio between different reactants [12,38]. With the vapor-based method, it is very difficult to measure the reaction rate precisely in a vacuum tube. Therefore, an accurate percentage ratio of the mixed perovskite film's components is measured by XPS, as well as XRD. The element components and distributions are shown in Fig. 3. The apparent Pb 4f, I 3d, and Br 3d characteristic peaks are used as references to analyze the ratio of different elements in the mixed perovskite films. First, Br 3d peaks, only, appear in the XPS spectrum of the $MA_xFA_{1-x}Pb\ (I_yBr_{1-y})_3$ film, as shown in Fig. 3(*c*). This demonstrates that the grown perovskite film fabricated by the HPCVD method with mixed MABr and FAI powder in the quartz tube contained Br ions. In addition, the grown perovskite films are halogen anion mixed perovskite films. Then, accurate ratios between organic cations or halogen anions were calculated by the XPS results in which a corrected relative sensitivity factor had already been applied to each element, as shown in Table 1. We can use the ratio between N and Pb to accurately calculate the ratio of MA and FA. Theoretically, each MA (CH_3NH_3) molecule contains one N atom and each FA ($CH(NH_2)_2$) contains two N atoms. As shown in Table 1, for the $MAPbI_3$ film without another organic cation, the measured ratio of N to Pb is 0.99, which is very close to the theoretical value of unity. Thus, this method is valid. Then we used this method to calculate the ratio of MA and FA cation in the $MA_xFA_{1-x}PbI_3$ and $MA_xFA_{1-x}Pb\ (I_yBr_{1-y})_3$ films. As shown in Table 1, the value of x in $MA_xFA_{1-x}PbI_3$ is 0.89 and the perovskite films can be derived as $MA_{0.89}FA_{0.11}PbI_3$. The value of x in the $MA_xFA_{1-x}Pb\ (I_yBr_{1-y})_3$ is 0.54 and the perovskite films can be derived as $MA_{0.54}FA_{0.46}Pb\ (I_yBr_{1-y})_3$. The ratio of I and Br can be directly obtained from Table 1. For the $MA_xFA_{1-x}Pb\ (I_yBr_{1-y})_3$ film, the value of y is 0.94 and $MA_xFA_{1-x}Pb\ (I_yBr_{1-y})_3$ can be derived as $MA_xFA_{1-x}Pb\ (I_{0.94}Br_{0.06})_3$. In summary, the three types of perovskite films, $MAPbI_3$, $MA_xFA_{1-x}PbI_3$, and

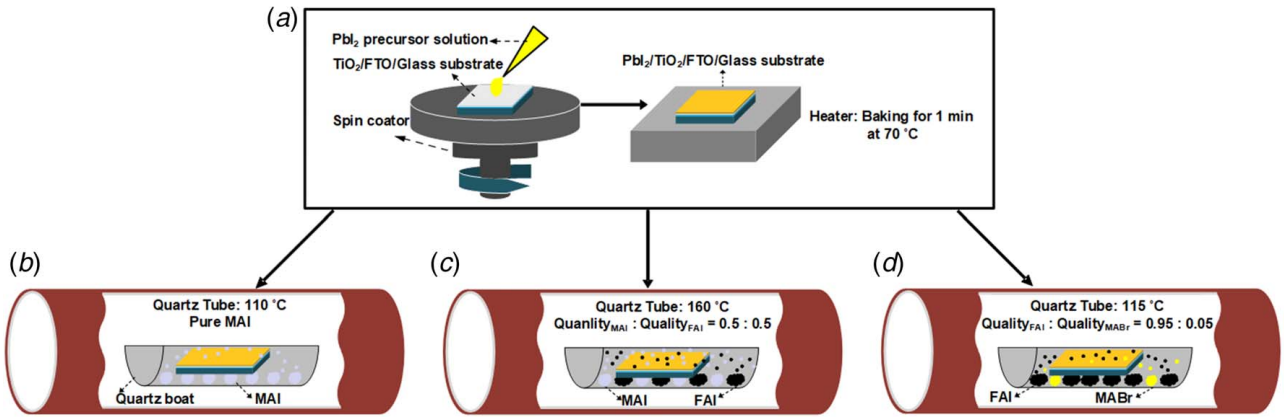

Fig. 2 Schematic diagram of the fabrication process for three different types of perovskite films ($MAPbI_3$, $MA_xFA_{1-x}PbI_3$, and $MA_xFA_{1-x}Pb\ (I_yBr_{1-y})_3$) by the HPCVD method: (*a*) fabrication of PbI_2 film, (*b*) growth of $MAPbI_3$ film by CVD method, (*c*) growth of $MA_xFA_{1-x}PbI_3$ film by CVD method, and (*d*) growth of $MA_xFA_{1-x}Pb\ (I_yBr_{1-y})_3$ film by CVD method

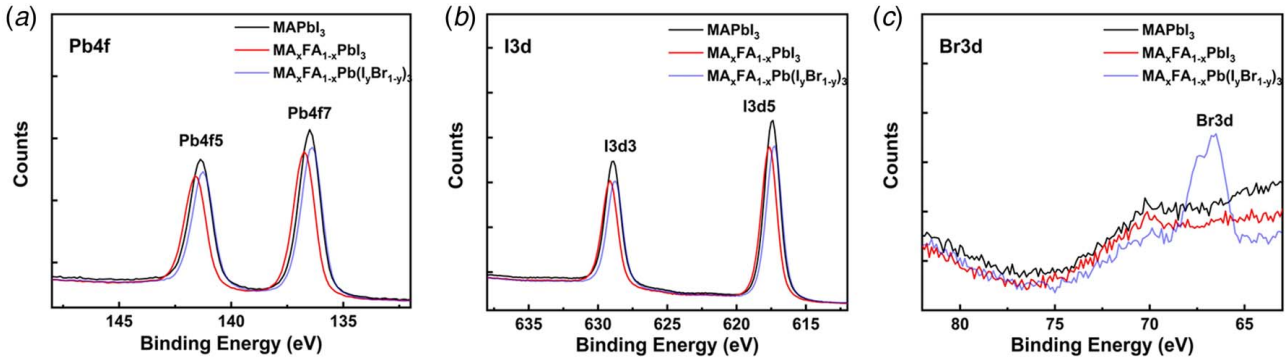

Fig. 3 XPS spectra of the three different types of perovskite films, $MAPbI_3$, $MA_xFA_{1-x}PbI_3$, and $MA_xFA_{1-x}Pb\ (I_yBr_{1-y})_3$ fabricated by the HPCVD method: (*a*) Pb 4f peak region, (*b*) I 3d peak region, and (c) Br 3d peak region

Table 1 Quantitative analysis of the atomic concentration of $MA_xFA_{1-x}Pb\ (I_yBr_{1-y})_3$ film by XPS with normalized Pb concentration

Perovskite film	N 1s	Br 3d	I 3d5	Pb 4f
$MAPbI_3$	0.99	0	2.84	1
$MA_xFA_{1-x}PbI_3$	1.11	0	2.77	1
$MA_xFA_{1-x}Pb\ (I_yBr_{1-y})_3$	1.46	0.16	2.70	1

$MA_xFA_{1-x}Pb\ (I_yBr_{1-y})_3$, can be derived as $MAPbI_3$, $MA_{0.89}FA_{0.11}PbI_3$, and $MA_{0.54}FA_{0.46}Pb\ (I_{0.94}Br_{0.06})_3$. In addition, from the XPS data for the three different kinds of perovskite films, as shown in Table 1, the ratios of Pb and anion (halogen ion) for the films are 1:2.84, 1:2.77, and 1:2.86. The three values are all close to but not exactly the theoretical value of 1:3. From the XRD results shown in Fig. 4, there is no PbI_2 residual in the three different kinds of perovskite films. We can conclude that the error regarding the ratio of Pb and halogen anions did not come from the PbI_2 residual. The reasons could be attributed to the XPS measurement process, the precision of the fitting process, decomposition of perovskite film, or possible diffusion of iodine in the perovskite material.

For the $MA_{0.54}FA_{0.46}Pb\ (I_{0.94}Br_{0.06})_3$ film, the reactants include PbI_2, FAI, and MABr. Therefore, if one MABr molecule or FAI molecule is fully involved in the reaction, the ratio of MA and Br and the ratio of FA and I, excluding the I ions coming from PbI_2, should be 1:1. However, the value we obtained from the XPS

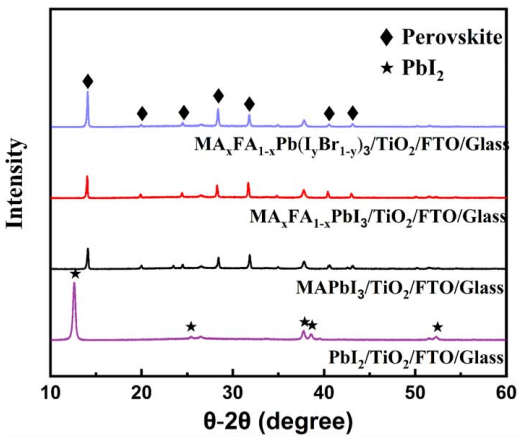

Fig. 4 XRD patterns of different types of films on TiO_2/FTO/glass, including PbI_2, $MAPbI_3$, $MA_xFA_{1-x}PbI_3$, and $MA_xFA_{1-x}Pb\ (I_yBr_{1-y})_3$

measurement regarding the ratio of MA to Br is 3:1 and the value for the ratio of FA to I, excluding the I ions coming from PbI_2, is 0.56:1. Neither were equal to the ratio in the reactants involved in the reaction. This suggests that there was a displacement reaction between different halogen ions in the CVD process. In addition, FA, MA, I, and Br ions were likely to be separately involved in the reaction, even though we used FAI and MABr as the reactants. To more precisely control the ratio between different ions in mixed $MA_xFA_{1-x}Pb\ (I_yBr_{1-y})_3$ films, more reactants, such as MAI and FABr, should be used in addition to FAI and MABr. Also, more reaction parameters, including temperature, vacuum level, and gas atmosphere should be optimized to achieve $MA_xFA_{1-x}Pb\ (I_yBr_{1-y})_3$ films with various sets of values for x and y. Further research is currently underway in our lab.

The bandgap of the mixed perovskite films fabricated by HPCVD were successfully adjusted by varying the reactant in the CVD process. The absorption spectrums of the three different types of perovskite films, including $MAPbI_3$, $MA_xFA_{1-x}PbI_3$, and $MA_xFA_{1-x}Pb\ (I_yBr_{1-y})_3$, are shown in Fig. 5(*a*). From Fig. 5, we find that the $MA_xFA_{1-x}PbI_3$ film has the highest absorbance intensity and the widest absorbance spectrum, followed by the $MAPbI_3$ film and the $MA_xFA_{1-x}Pb\ (I_yBr_{1-y})_3$ film, which has the narrowest absorbance spectrum. The bandgaps are estimated by using the absorption spectrums between 750 nm to 800 nm around the cutoff interval shown in Fig. 5(*b*). The $MA_xFA_{1-x}Pb\ (I_yBr_{1-y})_3$ film had the largest bandgap with a value about 1.61 eV, compared with 1.60 eV for the $MAPbI_3$ film and 1.58 eV for the $MA_xFA_{1-x}PbI_3$ film. The values may have some differences with the results obtained in the published results [5], but the trend is consistent with the reported results. Adjustable bandgaps of perovskite films fabricated by the HPCVD method can be achieved and the efficiency of PSCs based on the above films can be further optimized.

High performance PSCs were obtained based on the mixed perovskite films fabricated by HPCVD. The current density—voltage (J-V) curves of the highest efficiency of each of the PSCs with different types of perovskite films are shown in Fig. 6(*a*). Parameter values of these three kinds of PSCs, including PCE, short circuit current density (J_{sc}), open circuit voltage (V_{oc}), and fill factor (FF), are shown in Table 2. For the PSCs based on $MAPbI_3$, $MA_xFA_{1-x}PbI_3$ and $MA_xFA_{1-x}Pb\ (I_yBr_{1-y})_3$ films, PCE values of 14.5%, 16.4%, and 18.1% were obtained, respectively. Presented are PSCs based on each kind of perovskite film fabricated and measured. There are 14 perovskite solar cells for each of the three types. The sample-average PCE values for the three kinds of PSCs increased from 13.4% to 15.6% and 16.8%, as shown in Table 2. The efficiency distributions and performance parameters of the three kinds of PSCs are separately shown in Figs. 6(*b*) and 6(*c*).

Figure 6 shows that PSCs based on the $MA_xFA_{1-x}PbI_3$ have the highest short circuit current density (J_{sc}), about 23.3 mA/cm^2 for the champion solar cell. The reason can be attributed to its bandgap,

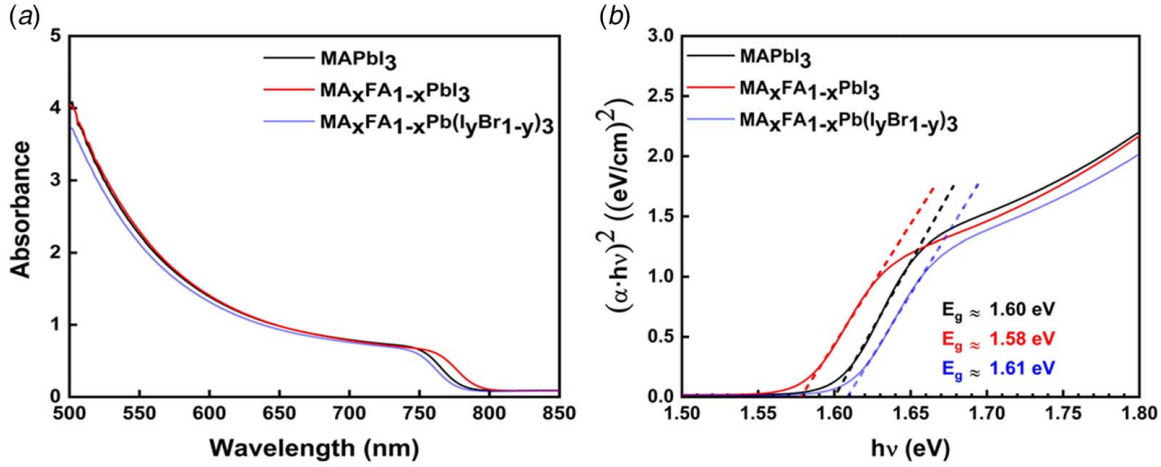

Fig. 5 (*a*) Absorbance spectrum of the three different types of perovskite films, $MAPbI_3$, $MA_xFA_{1-x}PbI_3$, and $MA_xFA_{1-x}Pb(I_yBr_{1-y})_3$, with wavelengths between 500 nm and 850 nm. (*b*) Derived bandgap of the three different types of perovskite films, $MAPbI_3$ (1.60 eV), $MA_xFA_{1-x}PbI_3$ (1.58 eV), and $MA_xFA_{1-x}Pb(I_yBr_{1-y})_3$ (1.61 eV), from the absorbance spectrum around the maximum light absorption wavelength.

which is the lowest, allowing it to absorb the widest spectrum, as noted above in Fig. 5. In addition, the top view SEM images of different types of perovskite films, $MAPbI_3$, $MA_xFA_{1-x}PbI_3$, and $MA_xFA_{1-x}Pb(I_yBr_{1-y})_3$ are shown in Fig. 7. From the SEM images, we can see that the morphology of the $MA_xFA_{1-x}PbI_3$ film is the most uniform. In addition, the $MA_xFA_{1-x}PbI_3$ films have the largest crystal size, which means that there are few grain boundary defects in the perovskite film, which is beneficial to the J_{sc}. Additionally, some reports state that $MA_xFA_{1-x}PbI_3$ films had enhanced crystallinity after FA ions incorporate into the $MAPbI_3$ crystal structure, which has a positive effect on J_{sc} [15]. Furthermore, as shown in Fig. 5(*b*), the $MA_xFA_{1-x}Pb(I_yBr_{1-y})_3$ film has a larger bandgap than the $MAPbI_3$ film, which means that the former can accommodate a narrower spectrum. However, the J_{sc} of PSCs based on $MA_xFA_{1-x}Pb(I_yBr_{1-y})_3$ film with the highest efficiency is larger than that based on $MAPbI_3$ film, 22.0 mA/cm^2 for the former and 21.3 mA/cm^2 for the latter. So were the average J_{sc} values; the former was 21.5 mA/cm^2 and the latter was for 20.8 mA/cm^2. The reason could be due to the Br ion, which can obviously decrease the defects in the perovskite films, as noted in the published results [15]. Jen's group showed that Br incorporated into a perovskite film can reduce the Pb_I antisites and help improve iodine-poor conditions. At the same time, they demonstrated that Br incorporated into the perovskite film can reduce the number of deep trap states coming from the defects or grain boundaries [15,39] in the perovskite material. In summary, compared with the other two

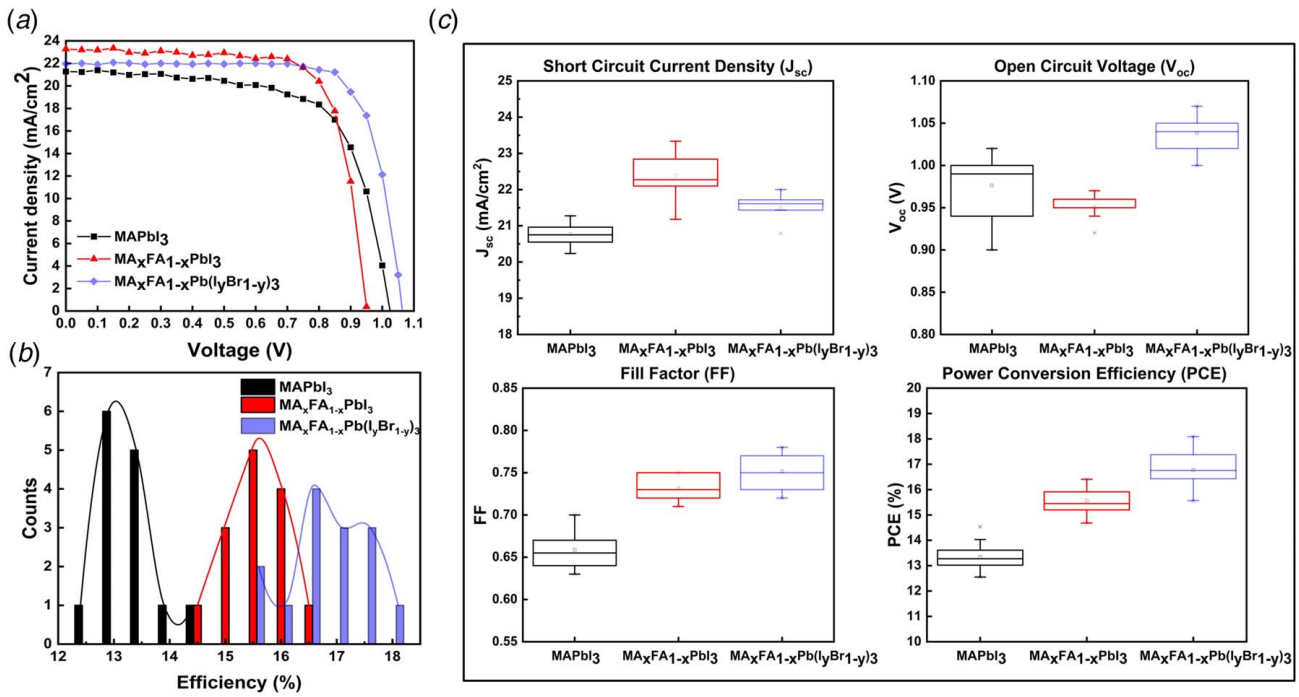

Fig. 6 (*a*) Current density–voltage (J-V) curves of the highest efficiency PSCs with different types of perovskite films, including $MAPbI_3$, $MA_xFA_{1-x}PbI_3$, and $MA_xFA_{1-x}Pb(I_yBr_{1-y})_3$. (*b*) Statistics of the efficiencies of PSCs based on the three different types of perovskite films. (*c*) Performance of the PSCs based on the three different types of perovskite films. The average PCE increased from 13.4% to 15.6% and 16.8%. Detailed information is shown in Table 2.

Table 2 Statistics of PSCs based on three different types of perovskite films including $MAPbI_3$, $MA_xFA_{1-x}PbI_3$, and $MA_xFA_{1-x}Pb(I_yBr_{1-y})_3$ fabricated by the HPCVD method

Perovskite	Types	PCE (%)	J_{sc} (mA/cm^2)	V_{oc} (V)	FF
$MAPbI_3$	Maximum	14.5	21.3	1.02	0.67
$MAPbI_3$	Mean	13.4	20.8	0.98	0.66
$MA_xFA_{1-x}PbI_3$	Maximum	16.4	23.3	0.94	0.75
$MA_xFA_{1-x}PbI_3$	Mean	15.6	22.4	0.95	0.73
$MA_xFA_{1-x}Pb(I_yBr_{1-y})_3$	Maximum	18.1	22.0	1.06	0.78
$MA_xFA_{1-x}Pb(I_yBr_{1-y})_3$	Mean	16.8	21.5	1.04	0.75

kinds of perovskite films, the $MA_xFA_{1-x}Pb(I_yBr_{1-y})_3$ film has the largest bandgap and the narrowest absorption spectrum, as shown in Fig. 5. In addition, the $MA_xFA_{1-x}Pb(I_yBr_{1-y})_3$ film has the worst surface morphology and smallest crystal size, as shown in Fig. 7. Despite this, the PSCs based on a $MA_xFA_{1-x}Pb(I_yBr_{1-y})_3$ film can still have a high J_{sc} value.

For the V_{oc}, PSCs based on a $MA_xFA_{1-x}Pb(I_yBr_{1-y})_3$ film have a high value of 1.06 V for the best performance solar cell and a value of 1.04 V for the average. The value for the PSCs based on an $MA_xFA_{1-x}PbI_3$ film is 0.94 V for the champion solar cell and 0.95 V for average. Lastly, the value for the PSCs based on an $MAPbI_3$ film is 1.02 V for the champion solar cell and 0.98 V for average. The most important reason may be the difference between energy bands for each kind of perovskite film, as shown in Fig. 5(*b*). The $MA_xFA_{1-x}Pb(I_yBr_{1-y})_3$ film has the largest V_{oc} value at 1.61 eV, compared with 1.60 eV for $MAPbI_3$ film and 1.58 eV for the $MA_xFA_{1-x}PbI_3$ film. This trend corresponds to the trend of V_{oc} in our experimental results.

Another phenomenon observed in our experimental results is that the fill factor (FF) has a huge improvement over those fabricated as mixed perovskite films with the HPCVD method. As discussed in our previous work [18], for the PSCs based on $MAPbI_3$ films fabricated by HPCVD method, we can increase the FF by increasing the spin coating speed of the PbI_2/DMF solution. However, along with the increased FF, the thickness of the perovskite film decreases, which leads to a drop in the light absorbance efficiency. However, in our study, the PSCs with the highest efficiency that are based on the $MA_xFA_{1-x}PbI_3$ and $MA_xFA_{1-x}Pb(I_yBr_{1-y})_3$ films can have a huge FF of 0.75 and 0.78, respectively, without a subsequent decrease of film thickness. The trend of average FF for three kinds of PSCs is shown in Fig. 6(*c*). Compared with the PSCs based on $MAPbI_3$ films, the FFs of the solar cells based on $MA_xFA_{1-x}PbI_3$ films show a major improvement. The reason may be the improved surface morphology and enhanced crystallization of the $MA_xFA_{1-x}PbI_3$ films, as shown in Fig. 7. For the PSCs based on a $MA_xFA_{1-x}Pb(I_yBr_{1-y})_3$ film, the FF is also further improved. Another reason may be due to Br ion inserted into the perovskite film. In addition to the reason mentioned above, Kim et al. had found that insertion of Br ions into $MAPbI_3$ can reduce the potential barrier at the apparent grain boundary [40]. This can help to enhance the FF by improving carrier collection while suppressing recombination.

Also, we conducted detailed research about PSCs based on $MA_xFA_{1-x}Pb(I_yBr_{1-y})_3$ film to identify the reasons for their excellent performance. A tapping-mode AFM height image of the PbI_2 film, the perovskite ($MA_xFA_{1-x}Pb(I_yBr_{1-y})_3$) film and the perovskite ($MAPbI_3$) film are shown in Fig. 8. Figure 8(*a*) shows that the root-mean-square (RMS) of the surface roughness of the PbI_2/TiO_2/FTO/glass substrate is only 4.4 nm, for an area of $5 \times 5\ \mu m$. Figure 8(*b*) describes the surface roughness of the $MA_xFA_{1-x}Pb(I_yBr_{1-y})_3$ /TiO_2/FTO/glass substrate fabricated by the HPCVD method. It is only 14.7 nm, for an area of $5 \times 5\ \mu m$. This is smaller than the $MAPbI_3$ film fabricated by the same process with an RMS of 17.4 nm, as shown in Fig. 8(*c*). In addition, the value of 14.7 nm is also significantly smaller than some published results [41–43]. The nonuniform surface has many negative effects on the interface characteristics. First, it would increase the carrier surface recombination at the interface between the perovskite film and the electron/hole transport layers, which would greatly decrease the performance of the device [42]. In addition, the nonuniform surface will poorly influence the spin coating process. For the PSCs fabricated in this paper, the film on the top of perovskite film was of Spiro-OMeTAD, which also was fabricated by the spin coating method. So, the nonuniform surface would result in poor quality of the Spiro-OMeTAD film. These may be the reasons why our PSCs had higher efficiency than others fabricated by a similar method. However, the perovskite solar cell with both FA^+ and Br^- mixed $MA_xFA_{1-x}Pb(I_yBr_{1-y})_3$ film had the best performance, with an efficiency of 18.1%, but with a poorer film quality, as shown in Fig. 7. We speculate that the growth rate caused by different temperatures during growth in the CVD process would be one main reason for the different surface morphologies. Another reason could be due to the different physical properties, such as boiling point and sublimation rate, of the different reactants that were used. In addition, more reactants involved in the reaction would lead to more uncontrollable variables in the growth process of the perovskite films. Furthermore, the vapor-based growth of fabricating compositional perovskite films must be optimized. A method to precisely control the ratio of different elements in the $MA_xFA_{1-x}Pb(I_yBr_{1-y})_3$ film must be found. With further improvement, we believe that a higher efficiency of PSCs based on $MA_xFA_{1-x}Pb(I_yBr_{1-y})_3$ films will be achieved.

Note that, for a planar structure perovskite solar cell with TiO_2 as the electron transport layer, hysteresis is still more pronounced than with a mesoporous structure or with inverted structure PSCs [44,45]. As mentioned before, PSCs with a planar structure have a huge hysteresis, with a PCE of 14.4% for a reverse scan and a PCE of 9.7% for a forward scan [18]. However, when we used $MA_xFA_{1-x}Pb(I_yBr_{1-y})_3$ to replace $MAPbI_3$ in the PSCs with the same structure, the hysteresis was vastly reduced. As shown in Fig. 9, PSCs based on $MA_xFA_{1-x}Pb(I_yBr_{1-y})_3$ films have better

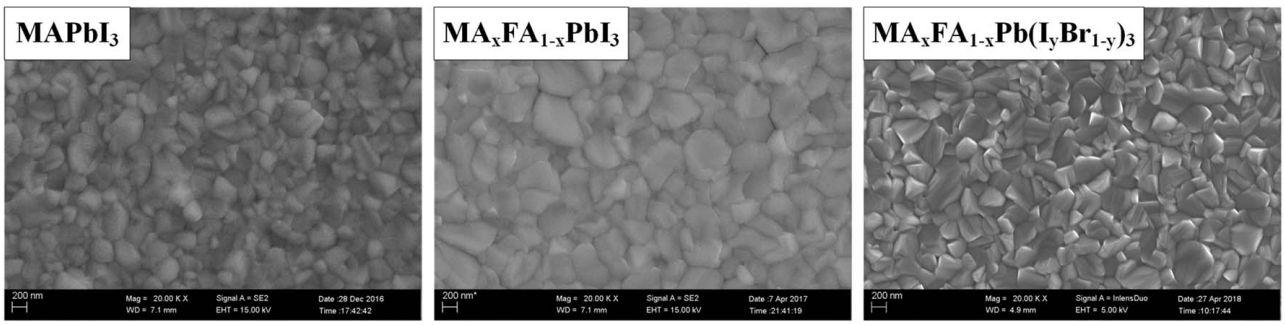

Fig. 7 Top view SEM images of different types of perovskite films, including $MAPbI_3$, $MA_xFA_{1-x}PbI_3$, and $MA_xFA_{1-x}Pb(I_yBr_{1-y})_3$, from left to right, fabricated by the HPCVD method

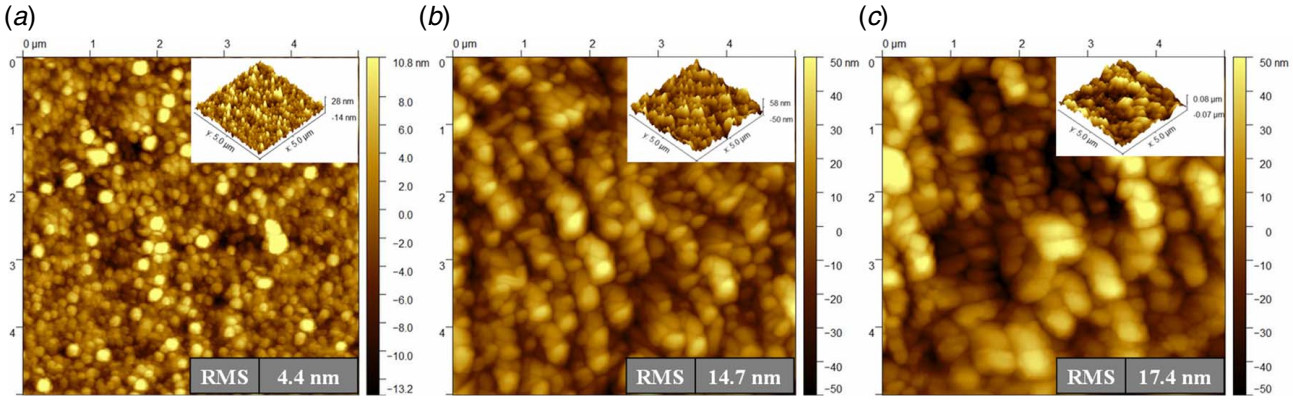

Fig. 8 Tapping-mode AFM height image of the PbI_2 film (*a*) fabricated by spin coating PbI_2/DMF + DMSO (volume ratio is 95:5) solution with surface roughness of about RMS 4.4 nm, the perovskite ($MA_xFA_{1-x}Pb$ (I_yBr_{1-y})$_3$) film, (*b*) fabricated by the HPCVD method with surface roughness of about RMS 14.7 nm, and the perovskite ($MAPbI_3$) film, and (*c*) fabricated by the HPCVD method with surface roughness of about RMS 17.4 nm, as a comparison

performance, with a reverse scan: $J_{sc} = 22.0$ mA/cm^2, $V_{oc} = 1.06$ V, FF = 0.78, and PCE = 18.1%; and a forward scan: $J_{sc} = 21.8$ mA/cm^2, $V_{oc} = 1.05$ V, FF = 0.73, and PCE = 16.6%. It is believed that ion (or defect) migration is closely related to hysteresis in PSCs, as well as the bulk or surface defects and ferroelectric properties of perovskite [44]. One reason why the hysteresis was greatly improved may be explained by the different perovskite compositions that can lead to different iodide defects and ion migration barriers. Oranskaia et al. found that PSCs based on FA-containing perovskite films have smaller hysteresis characteristics than those based on MA-containing perovskite films, because of the higher activation energy barrier of the FA-containing perovskite film [46]. Another reason why PSCs based on $MA_xFA_{1-x}Pb$ (I_yBr_{1-y})$_3$ films have smaller hysteresis characteristics can be attributed to a decrease of the bulk or surface defects in perovskite films caused by the insertion of FA and Br ions into $MAPbI_3$, as noted above [44]. However, the hysteresis in our PSCs based on $MA_xFA_{1-x}Pb$ (I_yBr_{1-y})$_3$ films still exists. Correa Baena et al. have chosen SnO_2 to replace TiO_2 as the electron transport layer in planar structured PSCs [47]. Using this method, they achieved nearly hysteresis-free PSCs with a PCE of 18.4% for a reverse scan and a PCE of 18.1% for a forward scan. Passivation layers on the upper or lower surface of perovskite film were believed to be an effective method to reduce the hysteresis in PSCs by decreasing the interface defects and surface recombination [7,48]. To be noted, an effective passivation layer must be ultrathin and very uniform, so the usual fabrication methods such as spin coating are not very proper [7,48]. Some nano-manufacturing methods [49] such as self-assembly and spray coating [50] could be used to fabricate high-quality passivation layers. We believe hysteresis in our fabricated PSCs can be further improved when different electron/hole transport layers are chosen to replace the currently used set: TiO_2 and Spiro-OMeTAD [45], or high-quality passivation layers are fabricated.

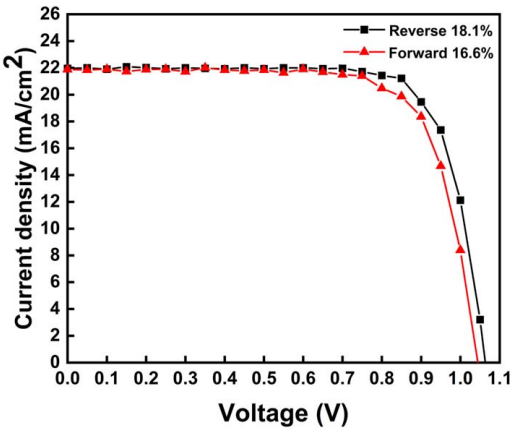

Fig. 9 Current density–voltage (J-V) curves of the champion perovskite solar cell based on an $MA_xFA_{1-x}Pb$ (I_yBr_{1-y})$_3$ film

Conclusion

In summary, a hybrid physical–chemical vapor deposition method was used to successfully fabricate perovskite films with adjustable components and bandgaps, such as $MAPbI_3$, $MA_{0.89}FA_{0.11}PbI_3$ and $MA_{0.54}FA_{0.46}Pb$ ($I_{0.94}Br_{0.06}$)$_3$. The adjustable bandgaps of these three perovskite films are 1.60 eV, 1.58 eV, and 1.61 eV, respectively. To our knowledge, this is the first time PSCs have been fabricated with halogen anion mixed perovskite films. PSCs based on $MA_{0.54}FA_{0.46}Pb$ ($I_{0.94}Br_{0.06}$)$_3$ achieved a high efficiency of 18.1%. Details regarding the vapor-based growth process research for compositional perovskite films and the methods to precisely control the ratio of different elements are discussed. We believe that PSCs with $MA_xFA_{1-x}Pb$ (I_yBr_{1-y})$_3$ will have higher efficiency and more stability in the future. In the meantime, our subsequent work will be to help develop a more competitive method to fabricate high-performance, large-area and low-cost PSCs in large-scale production to help promote commercial applications of PSCs.

Conflict of Interest

There are no conflicts of interest.

References

[1] The National Renewable Energy Laboratory (NREL), 2019, https://www.nrel.gov/pv/assets/pdfs/best-research-cell-efficiencies.20190802.pdf.
[2] Kojima, A., Teshima, K., Shirai, Y., and Miyasaka, T., 2009, "Organometal Halide Perovskites as Visible-Light Sensitizers for Photovoltaic Cells," J. Am. Chem. Soc., **131**(17), pp. 6050–6051.
[3] Xiao, J.-W., Liu, L., Zhang, D., De Marco, N., Lee, J.-W., Lin, O., Chen, Q., and Yang, Y., 2017, "The Emergence of the Mixed Perovskites and Their Applications as Solar Cells," Adv. Energy Mater., **7**(20), p. 1700491.
[4] Nelson, J., 2003, *The Physics of Solar Cells*, Imperial College Press, London.
[5] Eperon, G. E., Stranks, S. D., Menelaou, C., Johnston, M. B., Herz, L. M., and Snaith, H. J., 2014, "Formamidinium Lead Trihalide: A Broadly Tunable Perovskite for Efficient Planar Heterojunction Solar Cells," Energy Environ. Sci., **7**(3), pp. 982–988.
[6] Jung, H. S., and Park, N.-G., 2015, "Perovskite Solar Cells: From Materials to Devices," Small, **11**(1), pp. 10–25.
[7] Jiang, Q., Zhao, Y., Zhang, X., Yang, X., Chen, Y., Chu, Z., Ye, Q., Li, X., Yin, Z., and You, J., 2019, "Surface Passivation of Perovskite Film for Efficient Solar Cells," Nat. Photonics., **13**(7), pp. 460–466.

[8] Saliba, M., Correa-Baena, J.-P., Wolff, C. M., Stolterfoht, M., Phung, N., Albrecht, S., Neher, D., and Abate, A., 2018, "How to Make Over 20% Efficient Perovskite Solar Cells in Regular (n–i–p) and Inverted (p–i–n) Architectures," Chem. Mater., **30**(13), pp. 4193–4201.

[9] Jeon, N. J., Na, H., Jung, E. H., Yang, T.-Y., Lee, Y. G., Kim, G., Shin, H.-W., Il Seok, S., Lee, J., and Seo, J., 2018, "A Fluorene-Terminated Hole-Transporting Material for Highly Efficient and Stable Perovskite Solar Cells," Nat. Energy., **3**(8), pp. 682–689.

[10] Jiang, Q., Chu, Z., Wang, P., Yang, X., Liu, H., Wang, Y., Yin, Z., Wu, J., Zhang, X., and You, J., 2017, "Planar-Structure Perovskite Solar Cells with Efficiency Beyond 21," Adv. Mater., **29**(46), p. 1703852.

[11] Kim, M., Kim, G.-H., Lee, T. K., Choi, I. W., Choi, H. W., Jo, Y., Yoon, Y. J., Kim, J. W., Lee, J., Huh, D., Lee, H., Kwak, S. K., Kim, J. Y., and Kim, D. S., 2019, "Methylammonium Chloride Induces Intermediate Phase Stabilization for Efficient Perovskite Solar Cells," Joule, **3**(9), pp. 2179–2192.

[12] Salado, M., Calio, L., Berger, R., Kazim, S., and Ahmad, S., 2016, "Influence of the Mixed Organic Cation Ratio in Lead Iodide Based Perovskite on the Performance of Solar Cells," Phys. Chem. Chem. Phys., **18**(39), pp. 27148–27157.

[13] Lee, J. W., Seol, D. J., Cho, A. N., and Park, N. G., 2014, "High-Efficiency Perovskite Solar Cells Based on the Black Polymorph of $HC(NH_2)_2$ PbI_3," Adv. Mater., **26**(29), pp. 4991–4998.

[14] Pellet, N., Gao, P., Gregori, G., Yang, T. Y., Nazeeruddin, M. K., Maier, J., and Gratzel, M., 2014, "Mixed-Organic-Cation Perovskite Photovoltaics for Enhanced Solar-Light Harvesting," Angew. Chem. Int. Ed. Engl., **53**(12), pp. 3151–3157.

[15] Yang, Z., Chueh, C.-C., Liang, P.-W., Crump, M., Lin, F., Zhu, Z., and Jen, A. K. Y., 2016, "Effects of Formamidinium and Bromide Ion Substitution in Methylammonium Lead Triiodide Toward High-Performance Perovskite Solar Cells," Nano Energy, **22**, pp. 328–337.

[16] Yang, M., Zhang, T., Schulz, P., Li, Z., Li, G., Kim, D. H., Guo, N., Berry, J. J., Zhu, K., and Zhao, Y., 2016, "Facile Fabrication of Large-Grain $CH_3NH_3PbI_3$-XBrx Films for High-Efficiency Solar Cells via CH_3NH_3Br-Selective Ostwald Ripening," Nat. Commun., **7**(1), p. 12305.

[17] Green, M. A., Ho-Baillie, A., and Snaith, H. J., 2014, "The Emergence of Perovskite Solar Cells," Nat. Photonics, **8**(7), pp. 506–514.

[18] Wei, X., Peng, Y., Jing, G., and Cui, T., 2018, "Planar Structured Perovskite Solar Cells by Hybrid Physical Chemical Vapor Deposition With Optimized Perovskite Film Thickness," Jpn. J. Appl. Phys., **57**(5), p. 052301.

[19] Burschka, J., Pellet, N., Moon, S. J., Humphry-Baker, R., Gao, P., Nazeeruddin, M. K., and Gratzel, M., 2013, "Sequential Deposition as a Route to High-Performance Perovskite-Sensitized Solar Cells," Nature, **499**(7458), pp. 316–319.

[20] Im, J.-H., Jang, I.-H., Pellet, N., Grätzel, M., and Park, N.-G., 2014, "Growth of $CH_3NH_3PbI_3$ Cuboids With Controlled Size for High-Efficiency Perovskite Solar Cells," Nat. Nanotechnol., **9**(11), pp. 927–932.

[21] Liu, M., Johnston, M. B., and Snaith, H. J., 2013, "Efficient Planar Heterojunction Perovskite Solar Cells by Vapour Deposition," Nature, **501**(7467), pp. 395–398.

[22] Chen, C. W., Kang, H. W., Hsiao, S. Y., Yang, P. F., Chiang, K. M., and Lin, H. W., 2014, "Efficient and Uniform Planar-Type Perovskite Solar Cells by Simple Sequential Vacuum Deposition," Adv. Mater., **26**(38), pp. 6647–6652.

[23] Leyden, M. R., Ono, L. K., Raga, S. R., Kato, Y., Wang, S., and Qi, Y., 2014, "High Performance Perovskite Solar Cells by Hybrid Chemical Vapor Deposition," J. Mater. Chem. A., **2**(44), pp. 18742–18745.

[24] Chen, Q., Zhou, H., Song, T. B., Luo, S., Hong, Z., Duan, H. S., Dou, L., Liu, Y., and Yang, Y., 2014, "Controllable Self-Induced Passivation of Hybrid Lead Iodide Perovskites Toward High Performance Solar Cells," Nano Lett., **14**(7), pp. 4158–4163.

[25] Li, Y., Cooper, J. K., Buonsanti, R., Giannini, C., Liu, Y., Toma, F. M., and Sharp, I. D., 2015, "Fabrication of Planar Heterojunction Perovskite Solar Cells by Controlled Low-Pressure Vapor Annealing," J. Phys. Chem. Lett., **6**(3), pp. 493–499.

[26] Ono, L. K., Leyden, M. R., Wang, S., and Qi, Y., "Organometal Halide Perovskite Thin Films and Solar Cells by Vapor Deposition," J. Mater. Chem. A., **4**(18), pp. 6693–6713.

[27] Conings, B., Baeten, L., De Dobbelaere, C., D'Haen, J., Manca, J., and Boyen, H. G., 2014, "Perovskite-Based Hybrid Solar Cells Exceeding 10% Efficiency With High Reproducibility Using a Thin Film Sandwich Approach," Adv. Mater., **26**(13), pp. 2041–2046.

[28] Mitzi, D. B., Prikas, M., and Chondroudis, K., 1999, "Thin Film Deposition of Organic–Inorganic Hybrid Materials Using a Single Source Thermal Ablation Technique," Chem. Mater., **11**(3), pp. 542–544.

[29] Liang, P.-W., Liao, C.-Y., Chueh, C.-C., Zuo, F., Williams, S. T., Xin, X.-K., Lin, J., and Jen, A. K. Y., 2014, "Additive Enhanced Crystallization of Solution-Processed Perovskite for Highly Efficient Planar-Heterojunction Solar Cells," Adv. Mater., **26**(22), pp. 3748–3754.

[30] Jeon, N. J., Noh, J. H., Kim, Y. C., Yang, W. S., Ryu, S., and Seok, S. I., 2014, "Solvent Engineering for High-Performance Inorganic–Organic Hybrid Perovskite Solar Cells," Nat. Mater., **13**(9), pp. 897–903.

[31] Singh, T., and Miyasaka, T., 2017, "Stabilizing the Efficiency Beyond 20% With a Mixed Cation Perovskite Solar Cell Fabricated in Ambient Air Under Controlled Humidity," Adv. Energy Mater., **8**(3), p. 1700677.

[32] Shen, P.-S., Chen, J.-S., Chiang, Y.-H., Li, M.-H., Guo, T.-F., and Chen, P., 2016, "Low-Pressure Hybrid Chemical Vapor Growth for Efficient Perovskite Solar Cells and Large-Area Module," Adv. Mater. Interfaces, **3**(8), p. 1500849.

[33] Peng, Y., Jing, G., and Cui, T., 2015, "A Hybrid Physical–Chemical Deposition Process at Ultra-Low Temperatures for High-Performance Perovskite Solar Cells," J. Mater. Chem. A, **3**(23), pp. 12436–12442.

[34] Zhu, R., Wei, X., Xie, G., Simon, T., and Cui, T., 2020, "Numerical Simulation of Vapor Deposition Process of Perovskite Solar Cells: The Influence of Methylammonium Iodide Vapor Flow to Perovskite Growth," ASME J. Sol. Energy Eng., **143**(1), p. 011002.

[35] Chen, J., Xu, J., Xiao, L., Zhang, B., Dai, S., and Yao, J., 2017, "Mixed-Organic-Cation $(FA)_x(MA)_{1-x}PbI_3$ Planar Perovskite Solar Cells With 16.48% Efficiency via a Low-Pressure Vapor-Assisted Solution Process," ACS Appl. Mater. Interfaces, **9**(3), pp. 2449–2458.

[36] Jiang, Y., Leyden, M. R., Qiu, L., Wang, S., Ono, L. K., Wu, Z., Juarez-Perez, E. J., and Qi, Y., 2018, "Combination of Hybrid CVD and Cation Exchange for Upscaling Cs-Substituted Mixed Cation Perovskite Solar Cells With High Efficiency and Stability," Adv. Funct. Mater., **28**(1), p. 1703835.

[37] Zhu, X., Yang, D., Yang, R., Yang, B., Yang, Z., Ren, X., Zhang, J., Niu, J., Feng, J., and Liu, S., 2017, "Superior Stability for Perovskite Solar Cells With 20% Efficiency Using Vacuum Co-Evaporation," Nanoscale, **9**(34), pp. 12316–12323.

[38] Cui, P., Wei, D., Ji, J., Huang, H., Jia, E., Dou, S., Wang, T., Wang, W., and Li, M., 2019, "Planar p–n Homojunction Perovskite Solar Cells With Efficiency Exceeding 21.3%," Nat. Energy, **4**(2), pp. 150–159.

[39] Yin, W. J., Shi, T., and Yan, Y., 2014, "Unique Properties of Halide Perovskites as Possible Origins of the Superior Solar Cell Performance," Adv. Mater., **26**(27), pp. 4653–4658.

[40] Kim, G. Y., Oh, S. H., Nguyen, B. P., Jo, W., Kim, B. J., Lee, D. G., and Jung, H. S., 2015, "Efficient Carrier Separation and Intriguing Switching of Bound Charges in Inorganic-Organic Lead Halide Solar Cells," J. Phys. Chem. Lett., **6**(12), pp. 2355–2362.

[41] Chen, Q., Zhou, H., Hong, Z., Luo, S., Duan, H. S., Wang, H. H., Liu, Y., Li, G., and Yang, Y., 2014, "Planar Heterojunction Perovskite Solar Cells via Vapor-Assisted Solution Process," J. Am. Chem. Soc., **136**(2), pp. 622–625.

[42] Peng, Y., Jing, G., and Cui, T., 2015, "High-Performance Perovskite Solar Cells Fabricated by Vapor Deposition With Optimized PbI_2 precursor Films," RSC Adv., **5**(116), pp. 95847–95853.

[43] Gao, B., Meng, J., Lu, J., and Zhao, R., 2020, "$CH_3NH_3PbI_3$ Perovskite Solar Cells With Efficiency Over 22% Fabricated by Green Antisolvent Method," Mater. Lett., **274**, p. 127995.

[44] Kang, D. H., and Park, N. G., 2019, "On the Current-Voltage Hysteresis in Perovskite Solar Cells: Dependence on Perovskite Composition and Methods to Remove Hysteresis," Adv. Mater., **31**(34), p. e1805214.

[45] Chen, B., Yang, M., Priya, S., and Zhu, K., 2016, "Origin of J–V Hysteresis in Perovskite Solar Cells," J. Phys. Chem. Lett., **7**(5), pp. 905–917.

[46] Oranskaia, A., Yin, J., Bakr, O. M., Brédas, J.-L., and Mohammed, O. F., 2018, "Halogen Migration in Hybrid Perovskites: The Organic Cation Matters," J. Phys. Chem. Lett., **9**(18), pp. 5474–5480.

[47] Correa Baena, J. P., Steier, L., Tress, W., Saliba, M., Neutzner, S., Matsui, T., Giordano, F., Jacobsson, T. J., Srimath Kandada, A. R., Zakeeruddin, S. M., Petrozza, A., Abate, A., Nazeeruddin, M. K., Grätzel, M., and Hagfeldt, A., 2015, "Highly Efficient Planar Perovskite Solar Cells Through Band Alignment Engineering," Energy Environ. Sci., **8**(10), pp. 2928–2934.

[48] Wu, S., Zhang, J., Li, Z., Liu, D., Qin, M., Cheung, S. H., Lu, X., Lei, D., So, S. K., and Zhu, Z., 2020, "Modulation of Defects and Interfaces Through Alkylammonium Interlayer for Efficient Inverted Perovskite Solar Cells," Joule, **4**(6), pp. 1248–1262.

[49] Yeatman, E. M., Gramling, H. M., and Wang, E. N., 2017, "Introduction to the Special Topic on Nanomanufacturing," Microsyst. Nanoeng., **3**(1), p. 17079.

[50] Cassano, C. L., Georgiev, T. Z., and Fan, Z. H., 2017, "Using Airbrushes to Pattern Reagents for Microarrays and Paper-Fluidic Devices," Microsyst. Nanoeng., **3**(1), p. 17055.